DOE/ET-53088-276 IFSR #276

Nonlinear Dynamics of Tearing Modes in the Reversed Field Pinch

J. A. Holmes, B. A. Carreras, P. H. Diamond,
and *V. E. Lynch*

Oak Ridge National Laboratory
P. O. Box Y
Oak Ridge, Tennessee 37831

May 1987

Nonlinear dynamics of tearing modes in the reversed field pinch[a)]

J. A. Holmes, B. A. Carreras, P. H. Diamond,[b)] and V. E. Lynch

Oak Ridge National Laboratory
P.O. Box Y
Oak Ridge, Tennessee 37831

The results of investigations of nonlinear tearing-mode dynamics in reversed field pinch plasmas are described. The linear instabilities have poloidal mode number $m = 1$ and toroidal mode numbers $10 \lesssim n \lesssim 20$, and the resonant surfaces are therefore in the plasma core. The nonlinear dynamics result in dual cascade processes. The first process is a rapid $m = 1$ spectral broadening toward high n, with a simultaneous spreading of magnetic turbulence radially outward toward the field-reversal surface. Global $m = 0$ perturbations, which are driven to large amplitudes by the $m = 1$ instabilities, in turn trigger the $m = 1$ spectral broadening by back-coupling to the higher n. The second process is a cascade toward large m and is mediated by $m = 2$ modes. The $m = 2$ perturbations have the structure of localized, driven current sheets and nonlinearly stabilize the $m = 1$ modes by transferring $m = 1$ energy to small-scale dissipation. The calculated spectrum has many of the qualitative features observed in experiments.

PACS no.:

---

a) Research sponsored by the Office of Fusion Energy, U.S. Department of Energy, under contract DE-AC05-84OR21400 with Martin Marietta Energy Systems, Inc.

b) Institute for Fusion Studies, University of Texas at Austin, Texas 78712.

I. INTRODUCTION

The occurrence of large-scale magnetohydrodynamic (MHD) activity is commonly observed[1,2] in reversed field pinch (RFP) experiments. This activity, believed to be the manifestation of $m = 1$ tearing modes, has been linked to relaxation and configuration maintenance (the dynamo effect)[3–5] and may be responsible for the anomalous losses.[5] Unlike the tokamak configuration in which, during normal operation, there are at most one or two widely separated tearing instabilities, the RFP is characterized by the occurrence of many closely spaced, unstable modes. For this reason, the strong nonlinear interaction of tearing modes should be an important mechanism in reversed field pinches. Hence, the reversed field pinch provides an important and interesting site for the study of the nonlinear dynamics of tearing modes and of the generation and effects of their associated turbulence.

In previous work,[5,6] a new, nonlinear saturation mechanism, based on cascading to small scales initiated by the generation of stable $m = 2$ current sheets, was proposed and used to estimate field-reversal rates by using quasilinear theory. The theoretical methods used in this model were originally developed for the initial stages of the tokamak disruption by Carreras *et al.*[7] and extended to include turbulent effects by Diamond and coworkers.[8] The model predicts that the nonlinear coupling of a low-m instability to a background of modes will be stabilizing or destabilizing, depending on whether the sign of Δ' for the higher m driven modes is negative or positive in the evolved mean field. During the tokamak disruption, according to numerical calculations, this sign becomes positive at the onset of the disruption.[7] In the RFP [assuming $(m''; n'') = (2; 2n + 1)$ is the driven mode coupling the $(1; n)$ and $(1; n + 1)$ instabilities], the sign of Δ' remains negative throughout the calculation; this is consistent with the stabilization of the $m = 1$ instabilities by nonlinear interaction. In this stabilization, energy is transferred from the $m = 1$ instabilities to small-scale dissipation in a cascade generated by localized, driven $m = 2$ current sheets.

Previous studies of the nonlinear saturation mechanism used a full set of MHD equations and were restricted by time-step limitations to relatively small ($\lesssim 70$) numbers of interacting modes. Further, detailed studies of nonlinear saturation and relaxation mechanisms are presented in this work. These studies use a reduced set of equations derived for the RFP in cylindrical geometry, assuming a low-beta, force-free ordering.[4] With this model, only two equations must be advanced, rather than seven as in full MHD. Furthermore, since compressional and fast waves have been ordered out, the time-step size is restricted by the poloidal, rather than fast, Alfvén time. The dynamical behavior (both

linear and nonlinear) of these equations agrees well with that of a full set of MHD equations, including compressibility, for low-beta cases. Using these equations, we present here calculations containing up to 500 modes.

In these calculations, dual spectral-transfer processes are observed. The first process is a broadening of the $m = 1$ spectrum toward large n. This mechanism is mediated by the radially extended $(m = 0; n = 1)$ mode which, when nonlinearly driven to large amplitude, back-couples to excite larger n, $m = 1$ modes. This spectral-transfer process redistributes energy among the $m = 1$ modes and results in an expansion of the zone of turbulence from the plasma core toward the field-reversal surface. One consequence of this is the possibility for "locking in" of field reversal driven by nonlinear processes (dynamo effect). The second process is a cascade to small scales and dissipation by progressive current filamentation. This mechanism is initiated by the nonlinear generation of stable $m = 2$ modes, which have the structure of localized current sheets. An interesting interplay occurs between these two spectral-transfer processes, since broadening the spectrum of $(m = 1; n)$ modes naturally results in increased "leakage" to small-scale dissipation via $(m' = 2; n' = 2n + 1)$ modes.

The remainder of this paper considers the behavior of the reduced set of equations (Sec. II), discusses of the equilibrium and computational assumptions (Sec. III), presents the nonlinear numerical results (Sec. IV), analyses the tearing-mode dynamics (Sec. V), and states our conclusions (Sec. VI).

II. THE REDUCED SET OF MHD EQUATIONS FOR THE REVERSED-FIELD PINCH

The calculations presented here are carried out by using a reduced set of resistive MHD equations derived for a force-free plasma in cylindrical geometry with periodic boundary conditions using an ordering scheme based on the assumption that instabilities grow slowly compared with an ideal MHD time scale.[4] The equations are written in dimensionless form with all lengths normalized to the minor radius a; magnetic fields, to the field strength B_0 on the magnetic axis; times, to the Alfvén time $\tau_A = a\sqrt{\mu_0\rho_0}/B_0$; mass density, to the magnetic axis value ρ_0; and resistivity η, to the axis value η_0. In the above expression, μ_0 is the vacuum magnetic permeability. In terms of these quantities, the effective inverse aspect ratio of the cylinder is given by $\varepsilon_L \equiv 2\pi a/L$, where L is the length, and the Lundquist number is $S \equiv \tau_R/\tau_A$, where $\tau_R = a^2\mu_0/\eta_0$ is the resistive skin time. The coordinate system is given by (r,θ,ς), where $0 \le r \le 1$ is the radius, $0 \le \theta \le 2\pi$ is the polar angle, and $0 \le \varsigma \le 2\pi$ is the axial length normalized to angular dimensions. A Fourier expansion is used in the polar and axial directions, assuming 2π periodicity in θ and ς, with m representing the polar number and n the axial mode number. Although the calculations are carried out in cylindrical geometry, we henceforth use the familiar toroidal geometry terms "poloidal" and "toroidal" to refer to the polar and axial mode numbers, respectively.

The model involves the separation of the evolution into equations for the average quantities [$(m = 0; n = 0)$ components] and for the fluctuations [$(m;n) \neq (0;0)$]. With the average field quantities expressed by brackets, $\langle\ \rangle$, and the fluctuations by the tilde, $\widetilde{\ }$, the fluctuations are represented by a velocity stream function, $\widetilde{\Phi}$, and two magnetic flux functions, $\widetilde{\Psi}$ and $\widetilde{\alpha}$, so that

$$\widetilde{\mathbf{v}} = \langle \mathbf{B} \rangle \times \vec{\nabla}\widetilde{\Phi}/|\langle \mathbf{B} \rangle|^2 \tag{1}$$

and

$$\widetilde{\mathbf{A}} = \widetilde{\Psi}\langle \mathbf{B} \rangle + \widetilde{\alpha}\hat{r} \tag{2}$$

are the fluctuating fluid velocity and vector potential, respectively. Here $\hat{r}$ is the unit vector in the radial direction. The evolution equation for the magnetic fluctuations is

$$\frac{\partial\widetilde{\Psi}}{\partial t} = -\frac{1}{|\langle \mathbf{B} \rangle|^2}\left(\langle \mathbf{B} \rangle + \widetilde{\mathbf{B}}\right) \cdot \vec{\nabla}\widetilde{\Phi} + \frac{\eta}{S}\widetilde{C}\ , \tag{3}$$

which is derived from the parallel component of Ohm's law. Here,

$$\widetilde{\mathbf{B}} = \vec{\nabla} \times \widetilde{\mathbf{A}} \tag{4}$$

is the magnetic field fluctuation;

$$\widetilde{C} = \frac{1}{|\langle \mathbf{B} \rangle|^2} \vec{\nabla} \cdot \left(|\langle \mathbf{B} \rangle|^2 \, \vec{\nabla} \widetilde{\Psi} - \langle \mathbf{B} \rangle \langle \mathbf{B} \rangle \cdot \vec{\nabla} \widetilde{\Psi} - \hat{r} \langle \mathbf{B} \rangle \cdot \vec{\nabla} \widetilde{\alpha} \right) \tag{5}$$

is the fluctuating current along the magnetic field; and the vector potential component, $\widetilde{\alpha}$, is given by the first-order force-free field assumption as

$$\left(\frac{1}{r^2} \frac{\partial^2}{\partial \theta^2} + \varepsilon_L^2 \frac{\partial^2}{\partial \zeta^2} \right) \widetilde{\alpha} = \langle \mathbf{B} \rangle \cdot \vec{\nabla} \frac{\partial}{\partial r} \widetilde{\Psi} \; . \tag{6}$$

The evolution of the velocity is determined by the vorticity equation

$$\begin{aligned} \frac{\partial}{\partial t} \widetilde{U} + \vec{\nabla} \cdot \left(\widetilde{U} \widetilde{\mathbf{v}} \right) + \vec{\nabla} \cdot \left(\vec{\nabla} \frac{|\widetilde{\mathbf{v}}|^2}{2} \times \langle \mathbf{B} \rangle \right) \\ = \mathbf{B} \cdot \vec{\nabla} \frac{\langle \mathbf{B} \rangle \cdot \langle \mathbf{J} \rangle}{|\langle \mathbf{B} \rangle|^2} - \mathbf{B} \cdot \vec{\nabla} \widetilde{C} \; , \end{aligned} \tag{7}$$

where

$$\langle \mathbf{J} \rangle = \vec{\nabla} \times \langle \mathbf{B} \rangle \tag{8}$$

is the current associated with the average field and

$$\widetilde{U} = \nabla^2 \widetilde{\Phi} \tag{9}$$

is the vorticity. The evolution of the average field is given by

$$\frac{\partial \langle \mathbf{B} \rangle}{\partial t} = \vec{\nabla} \times \left[\frac{\partial \langle A_{\parallel} \rangle}{\partial t} \langle \mathbf{B} \rangle + \frac{\partial \langle A_{\perp} \rangle}{\partial t} \left(\hat{r} \times \langle \mathbf{B} \rangle \right) \right] \; , \tag{10}$$

where $\partial \langle A_{\parallel} \rangle / \partial t$ is given by the parallel Ohm's law as

$$\frac{\partial \langle A_{\parallel} \rangle}{\partial t} = - \frac{1}{|\langle \mathbf{B} \rangle|^2} \langle \widetilde{\mathbf{B}} \cdot \vec{\nabla} \widetilde{\Phi} \rangle + \frac{1}{|\langle \mathbf{B} \rangle|^2} \langle \mathbf{B} \rangle \cdot \left(\mathbf{E}_{\ell} - \frac{\eta}{S} \langle \mathbf{J} \rangle \right) \tag{11}$$

and $\partial \langle A_{\perp} \rangle / \partial t$ is given by the assumption of force-free fields as

$$\begin{aligned} \frac{1}{r} \frac{\partial}{\partial r} \left(r |\langle \mathbf{B} \rangle|^2 \frac{\partial}{\partial r} \frac{\partial \langle A_{\perp} \rangle}{\partial t} \right) - \frac{\partial \langle A_{\perp} \rangle}{\partial t} \left(\frac{1}{r} \frac{\partial \langle B_{\theta} \rangle^2}{\partial r} + \frac{|\langle \mathbf{B} \rangle|^2}{r^2} \right) \\ = \frac{\partial}{\partial r} \left(\langle \mathbf{J} \rangle \cdot \langle \mathbf{B} \rangle \frac{\partial \langle A_{\parallel} \rangle}{\partial t} \right) - \frac{2 \langle B_{\theta} \rangle}{r} \frac{\partial}{\partial r} \left(\langle B_z \rangle \frac{\partial \langle A_{\parallel} \rangle}{\partial t} \right) \; . \end{aligned} \tag{12}$$

Here $\langle A_{\parallel} \rangle$ and $\langle A_{\perp} \rangle$ are the parallel and perpendicular components of the vector potential, respectively, and E_{ℓ} is the loop voltage.

Hence, there are essentially two evolution equations for each fluctuating mode, one for the magnetic flux function $\widetilde{\Psi}$ and one for the velocity stream function $\widetilde{\Phi}$, whereas the

average field is solved for independently. These equations represent a generalization of the reduced equations for low-beta tokamaks[9] to cases in which the toroidal magnetic field is not dominant. However, they strongly resemble the tokamak equations in their basic structure.

Consideration of the assumptions used to derive the reduced set of equations leads to the expectation that the dynamical behavior will be similar to that obtained in using a full set of MHD equations, including compressibility, at zero beta. For several cases in which a comparison has been made, this expectation has been fulfilled. Figure 1 shows the linear growth rate, at $S = 10^4$ and $\varepsilon_L = 0.2$, of the resistive $(m = 1; n)$ eigenmodes for the RFP equilibrium studied in this paper. The results of the reduced set of equations compare favorably with those calculated with the full compressible MHD equations (within 20%), whereas an incompressible calculation yields growth rates that are lower by more than a factor of 2. Comparison of the radial behavior of the eigenfunctions shows excellent agreement between the reduced set of equations and full MHD (Fig. 2), whereas the eigenfunctions obtained by using the incompressible model are different. The full MHD and the incompressible results were obtained by using the CYL code,[10] which was also used to carry out the calculations described in Ref. 6.

Another example, this time from a nonlinear calculation of a single helicity $m/n = 1/10$ tearing mode, is shown in Fig. 3. The agreement between the saturated magnetic island widths is within 20% ($W_{1/10} = 0.56a$ and $W_{1/10} = 0.46a$) for the reduced set and fully compressible equations, respectively. The growth of the magnetic island is somewhat delayed in the case using the full set of equations because of the smaller linear growth rate (see Fig. 1) and the small initial perturbation used in both calculations. Even so, the agreement between the two models is reasonably good. However, an incompressible calculation results in different behavior, in which the magnetic island grows much more slowly and the width saturates at only 22% of the minor radius. Hence, in these cases and others, the behavior of the reduced set of equations substantially agrees with that observed with full MHD at zero beta.

III. NUMERICAL CALCULATIONS: INITIAL EQUILBRIUM AND NUMERICAL METHOD

To study the nonlinear interaction of tearing modes in the RFP configuration, we have chosen a low-Θ equilibrium from Caramana *et al.*[3] (where Θ is defined as $B^{\theta}_{\text{edge}}/\{B\}$ and $\{B\}$ is the volume averaged toroidal field), which has several desirable features. First of all, since $\beta = 0$ for this equilibrium, the force-free assumption of the reduced equations is valid to the lowest order. This configuration also has aspect ratio $A_R = 5$ ($\varepsilon_L = 0.2$) and monotonically decreasing q profile, with values $q_0 = 0.1225$ on axis, $q_a = -0.0051$ at the edge, and $q = 0$ at $r_0 = 0.93$ determining the field-reversal surface. The equilibrium safety factor and current profiles are plotted in Fig. 4, where the arrows denote the resonant surfaces of the $m = 1$ instabilities. As seen in Fig. 1, this equilibrium is linearly stable to nonresonant $m = 1$ modes having $m/n > q_0 (n < 9)$ and also to high-n, $m = 1$ modes ($n > 21$). The linear eigenfunctions are calculated, as are all the results presented in this paper, at Lundquist number $S = 10^4$ with a constant resistivity profile. All modes other than those shown in Fig. 1 are linearly stable for this configuration. As shown in Fig. 4, the singular surfaces of the instabilities are closely spaced, but the $m = 1$ instabilities themselves, as shown in Fig. 2, are global in extent. Hence, this configuration provides the opportunity to study the strong nonlinear interaction of a number of closely spaced, globally structured, $m = 1$ tearing modes. This same equilibrium was used for most of the previous studies presented in Ref. 6.

Because of the large value of the resistivity (small Lundquist number $S = 10^4$) in these calculations and in RFP experiments, significant resistive diffusion of the average magnetic field occurs in a time comparable with the growth time of the tearing-mode fluctuations. Since the emphasis of the present work is on the nonlinear interaction of tearing modes, control of the resistive diffusion of the average field is desirable. For this reason, these calculations are carried out by replacing the term $\mathbf{E}_\ell - (\eta/S)\langle \mathbf{J} \rangle$ in Eq. (11) by $(\eta/S)\left(\langle \mathbf{J}(t=0) \rangle - \langle \mathbf{J} \rangle\right)$, where $\langle \mathbf{J}(t=0) \rangle$ is the initial average (equilibrium) current. With this expression, resistive diffusion tends to maintain the equilibrium as if it were a resistive equilibrium, and the tearing-mode interactions are the dominant dynamical processes. We stress that these computations should be viewed as a means for elucidation of basic physical processes, not as simulations of RFP plasmas.

The calculations are carried out with the computer code RPE (Reduced Pinch Equations), which solves the reduced set of equations in cylindrical geometry. Fourier expansion with periodic boundary conditions is used in the angle coordinates θ and ζ, and centered

finite differences with variable mesh spacing is used in r. One of the useful features of the RPE implementation of the reduced set of equations for RFPs is the ability to arbitrarily designate the set of fluctuations $(m;n)$ to be included in the calculation. This makes it possible to assess the effects of individual modes or groups of modes by including or deleting them from otherwise equivalent calculations. This capability was used extensively in this work to analyze the observed spectral broadening and cascade processes. All the choices described in this paragraph for the representation and implementation of the RPE equations are identical to those discussed in detail in Ref. 11 on the RSF code solution of the reduced set of tokamak equations.[9]

The time-advancement scheme used in this work is a partially implicit finite-difference method correct to the first order in step size. The equations can be advanced nonlinearly, or linear eigenfunctions can be obtained about the instantaneous average fields. Each physical quantity is defined at a single particular time; therefore, the occurrence of a quantity at the advanced or initial time in any particular term depends upon whether the equation for that quantity was previously advanced within the given time step. Such time-advancement schemes are minimal in their use of computer storage and are extremely simple to program. In the implementation used here, the fluctuations are advanced first, followed by the average-field equations. The procedure is as follows [for the fluctuations, each step is solved as a loop over the modes $(m;n)$]:

(1) Advance Eq. (7) explicitly to obtain $\widetilde{U}^+$.

(2) Solve Eqs. (9) and (1) for $\widetilde{\Phi}^+$ and $\widetilde{\mathrm{v}}^+$, respectively.

(3) Solve Eq. (3) for $\widetilde{\Psi}^+$. Evaluate the advective term explicitly, but note that $\widetilde{\Phi}^+$ appears because of step 2. Evaluate the resistive term implicitly in $\widetilde{\Psi}$, using Eqs. (5) and (6) to express the tridiagonal matrix form of $\widetilde{C}$ and $\widetilde{\alpha}$ in terms of $\widetilde{\Psi}$.

(4) Solve for $\widetilde{\alpha}$, using Eq. (6). This completes the time advancement of the fluctuating quantities.

(5) Solve Eq. (11) for $\partial\langle A_{\|}\rangle/\partial t$ explicitly. Note that $\mathbf{E}_\ell = (\eta/S)\langle\mathbf{J}(t=0)\rangle$ and that $\widetilde{\Phi}^+$ appears in the advective term.

(6) Solve Eq. (12) for $\partial\langle A_{\perp}\rangle/\partial t$ as a tridiagonal matrix equation.

(7) Solve Eq. (10) for $\langle\mathbf{B}\rangle^+$. To improve the numerical stability of this step, add $(\eta/S)\ \vec{\nabla}\times\langle\mathbf{J}\rangle$ to both sides of Eq. (10), evaluating this term implicitly on the left-hand side via tridiagonal matrix and explicitly on the right-hand side. This completes the first-order partially implicit time-advancement scheme.

For the boundary conditions, all quantities are required to have regular behavior at the origin; this implies for the fluctuations that $\widetilde{U}_{mn}$, $\widetilde{\Phi}_{mn}$, and $\widetilde{\Psi}_{mn} \sim r^{|m|}$ as $r \to 0$ and that $\widetilde{\alpha}_{mn} \sim r^{|m|+1}$. For the average fields, $\partial\langle A_{\|}\rangle/\partial t$ and $\langle B_z\rangle \sim a + br^2$, where a and b are

constants; $\partial\langle A_\perp\rangle/\partial t$ and $\langle B_\theta\rangle \sim r$; and $\langle B_r\rangle = 0$. At the conducting wall the boundary conditions are $B_r = v_r = 0$ which implies for the fluctuations that $\widetilde{\Phi}_{mn} = \widetilde{\Psi}_{mn} = 0$ at $r = 1$, whereas $\widetilde{\alpha}_{mn}$ is obtained by evaluation from Eq. (6). For the average fields, $\partial\langle A_\perp\rangle/\partial t$ is linearly extrapolated to the edge; $\langle B_\theta\rangle$ and $\langle B_z\rangle$ are required to maintain the initial edge current density, and therefore $1/r\,\partial/\partial r\,(r\langle B_\theta\rangle)_{r=1} = 1/r\partial/\partial r\,(r\langle B_\theta\rangle)_{r=1,t=0}$ and $\partial/\partial r\langle B_z\rangle_{r=1} = \frac{\partial}{\partial r}\langle B_z\rangle_{r=1,t=0}$.

The numerical convergence of these calculations as a function of the radial grid resolution depends on the problem being considered. For large values of S ($S \gtrsim 10^6$), several hundred unequally spaced radial points may be necessary to resolve the structure of the eigenfunctions and give converged solutions. However, for the calculations presented here at $S = 10^4$, 100 equally spaced radial grid points are sufficient to provide good resolution, even for the localized, driven, higher m modes. The issue of resolution in mode space is a more serious one for this problem, as seen in the following sections. Consistent with our previous experience with partially implicit, resistive, MHD initial-value codes,[10–12] the results are not very dependent on the time step-size as long as the calculation is numerically stable. It is advantageous, therefore, to use as large a step size as permitted by numerical stability requirements. In practice, we use the procedure described in Ref. 11 for controlling the size of the time step throughout the calculation.

IV. NONLINEAR CALCULATIONS: NUMERICAL RESULTS

For study of the nonlinear interaction and evolution of tearing modes numerically by using the reduced equations model with the equilibrium and assumptions described previously, calculations including up to 546 modes were carried out. Several of these calculations, which are considered here, are described in Table I. For the 546-mode calculation (Case 1 in Table I), poloidal mode numbers in the range $0 \leq m \leq 5$ were included. For $m = 1$, toroidal modes numbering $1 \leq n \leq 40$ were retained so that the linearly unstable modes $9 \leq n \leq 21$ could couple to higher and lower n. For $m = 0$, the average field $n = 0$ was retained, together with $1 \leq n \leq 15$, which provide coupling of the $m = 1$ instabilities. For $m = 2$ we retained $1 \leq n \leq 80$ (i.e., all harmonics of the $m = 1$ modes as well as all $m = 2$ modes that directly couple the $m = 1$ modes). In addition, the higher m modes $(m = 3; 1 \leq n \leq 120)$, $(m = 4; 1 \leq n \leq 140)$, and $(m = 5; 1 \leq n \leq 150)$ were retained to provide a turbulent background and a large-n energy sink. To initialize the calculations, all $m = 1$ perturbations were given comparable small magnetic fluctuation levels corresponding, for the resonant modes, to magnetic island widths of 10^{-3} the minor radius.

The total magnetic fluctuation energy for several of these calculations is plotted as a function of time in Fig. 5. This energy is defined by

$$E^B_{\text{tot}} = \sum_{(m;n)\neq(0;0)} E^B_{mn} \,, \tag{13}$$

where $E^B_{mn} = 1/2 \int |\mathbf{B}_{mn}|^2 \, dV$, with the integral taken over the plasma volume. Here, $\mathbf{B}_{mn}$ is the $(m;n)$ component of the magnetic field as given by Eqs. (2) and (4). For Case 1 (the 546-mode calculation), prior to $t = 500\,\tau_A$ the linearly unstable $m = 1$ modes grow exponentially. During this time the fluctuations are quite small, and nonlinear effects are negligible. The fluctuation energy spectrum is dominated by the few most rapidly growing $m = 1$ instabilities (Figs. 6 and 7), whereas the $m \neq 1$ fluctuations are small, linearly stable, and driven by the $m = 1$ instabilities. In Fig. 6, E_{1n} is plotted versus n; in Fig. 7 the plotted energies are defined as

$$E^B_m = \sum_n E^B_{mn} \,. \tag{14}$$

At about $t = 500\,\tau_A$, the dominant $m = 1$ instabilities (with $11 \leq n \leq 15$) have grown to sufficient size so that their magnetic islands overlap, generating a region of stochastic magnetic field (Fig. 8) and strong nonlinear effects. Subsequently, there is a

rapid broadening of the magnetic energy spectrum toward high toroidal mode number n, as shown for $m = 1$ in Fig. 6. This spectral broadening toward high n also occurs for $m \neq 1$, as shown for $m = 0$ and 2 in Fig. 9 and for $m = 5$ in Fig. 10. However, the $m = 1$ modes continue to dominate the energy spectrum, as shown in Fig. 7. In Fig. 9 the energy distribution widths are defined for each poloidal mode number m as

$$(\Delta n)^2 = \frac{\sum_n (n - \overline{n})^2 E^B_{mn}}{E^B_m} , \tag{15}$$

where

$$\overline{n} = \frac{\sum_n n E^B_{mn}}{E^B_m} , \tag{16}$$

and Δn is plotted, centered at $\overline{n}$. The broadening of the spectrum in toroidal mode number corresponds to an outward expansion of the turbulence toward the field-reversal surface. This is illustrated in Fig. 11, where the poloidal component $B^{\theta}_{(1;n)}$ is plotted for $n = 19,\ 21,\ 25$, and 29 at $t = 600\,\tau_A$. Although these modes are fairly broad, the amplitudes peak in the vicinity of the respective singular radii, which increase with n. With the magnetic energies of the $(1;n)$ modes assigned to their singular radii and then summed within radial bins of width 0.1, the radial energy spreading at $500\,\tau_A$ and $650\,\tau_A$ is illustrated in Fig. 12. The effect on the magnetic field is shown quite clearly in Fig. 8, where the stochastic region generated by the overlap of magnetic islands advances all the way to the field-reversal surface by the conclusion of the calculation. Figure 13, which plots the average of the parallel current

$$\mu \equiv \mathbf{B} \cdot \mathbf{J} / |\mathbf{B}|^2 \tag{17}$$

as a function of radius, shows the fluctuations in the parallel current to have significant value from the plasma core through the field-reversal surface, and a flattening effect in the region of dominant instabilities, $0.3 \lesssim r \lesssim 0.6$. Although the spectral broadening in toroidal mode number n (and in radius) is accompanied by some spectral broadening in poloidal mode number m, the energy remains primarily in the $m = 1$ modes, followed by $m = 0$ and $m = 2$, respectively (Fig. 7). The cascade to short wavelengths is accompanied by a nonlinear saturation of the total perturbation energy, as shown in Fig. 5. The initial equilibrium is evidently sufficiently close to a Taylor state[13] so that the induced instabilities fail to disrupt the plasma. Rather, as suggested by the field line plots of Fig. 8 and the spectral results, a turbulent, saturated quasi-steady state is reached. Figure 14 shows the time evolution of the $m = 1$ magnetic energy spectrum. Several features are worth noting. In particular, the division of the central peak into two peaks of higher and lower toroidal mode number n is followed by the domination of the lower n peak. Also, fluctuations

develop at high n at the later times. Although this calculation is not a simulation of an RFP experiment, the features of the spectral evolution just described are in good qualitative agreement with the time evolution of the magnetic fluctuation spectrum obtained from HBTX-1A by Hutchinson *et al.*[2]

From Fig. 5, it is apparent that the total magnetic energies of Case 2 (136 modes) and Case 3 (96 modes) differ little from the total energy of Case 1 until after $t = 600\,\tau_A$ and that even Case 4 (41 modes) follows the total energies of the others until almost $550\,\tau_A$. Although the physics rationale for the mode selections shown in Table I are described in the next section, it is appropriate to comment here concerning the convergence of these cases with increasing number of modes. The agreement of the four cases early in time is due to the fact that the fluctuations in all four cases were initialized identically and that the dominant process, the linear growth of the unstable $m = 1$ modes, is well represented in all four mode selections. The first calculation that ceases to agree with Case 1 is Case 4, the 41-mode calculation. Of the four cases, Case 4 is the only one without direct nonlinear coupling of the $m = 1$ instabilities, and the disagreement therefore arises when nonlinear coupling effects become important. Cases 2 and 3, which retain many of the nonlinear couplings, but not the effect of the $m \geq 3$ modes, agree well with Case 1 until the effects of these high m modes become important. For example, at $t = 600\,\tau_A$ the energy spectra of the $m = 0$, 1, and 2 modes are nearly indistinguishable between Case 1 and Case 2. As shown in Fig. 15, even at $t = 672\,\tau_A$ the $m = 1$ spectra of Cases 1 and 2 are quite similar. In the next section these results are discussed further in relation to the nonlinear dynamics of the mode interactions, but we note here that good agreement between the different calculations is obtained until dynamical interaction processes involving modes contained in some, but not all, calculations become important.

To test the effect of the initialization, we carried out another calculation (Case 6 of Table I), equivalent to Case 2 (the 136-mode run) except for the initialization. In this calculation, rather than initializing all $m = 1$ modes, we initialized only the $(1;10)$ and $(1;11)$ modes. Because the $(1;11)$ mode grows more rapidly than the $(1;10)$, the evolution in this calculation is found to be nearly identical to that of a $(1;11)$ single helicity calculation for more than $600\,\tau_A$. Eventually, however, coupling effects become strong as other nonlinearly generated instabilities "catch up" to the $(1;11)$, and the overall perturbation saturates at about $850\,\tau_A$, at the same total energy level as in Case 2. Furthermore, comparison of the spectra of these two calculations at the time of saturation reveals comparable levels, both in the peak modes $n \approx 10$ and in the high- n tail (Fig. 16). Even though the details of the evolution depend significantly on the choice of initial conditions, both calculations

eventually reach turbulent, quasi-steady states at comparable overall excitation level and with similar magnetic energy spectra.

V. ANALYSIS OF THE NONLINEAR CALCULATIONS

In analysing of the nonlinear evolution presented in Sec. IV, we concentrate on the mechanisms of two features of the evolution: (1) the broadening of the fluctuation spectrum in wave number and radius and (2) the saturation of the fluctuation energies to give a quasi-steady, turbulent state. The approach taken here is to analyze the effects of the various sets of modes by including and excluding them from otherwise equivalent calculations and by examining the properties of these modes in the nonlinear evolution. By then evaluating this information using the framework of renormalized spectrum evolution equations,[5,8] we obtain a description of the nonlinear processes. The limitations of this method stem from the complicated nature of the nonlinear processes being analyzed. In view of these limitations, we focus first on the spectral broadening of the $m = 1$ modes and seek to determine whether this is driven by the quasilinear effects of the evolution of the mean field or by direct nonlinear-mode-coupling effects. In Fig. 17, the linear growth rates of the $m = 1$ perturbations are plotted versus n for the initial equilibrium and for the evolved mean fields at $t = 600\,\tau_A$. The figure shows the stabilization of the dominant $n = 11$–14 modes due to quasilinear effects, together with a destabilization of $n < 10$ and a shifting of the instability curve out in n to $15 \leq n \leq 25$. This quasilinear effect is due to a flattening of the current gradient near the singular surfaces of the dominant instabilities (see Fig. 13), which leads to their stabilization, and an associated steepening of the current gradient both inside and outside the region of the resonant surfaces of the dominant instabilities, which leads to the observed destabilization of the modes having singular surfaces in these regions. Note, however, that, although quasilinear effects do lead to destabilization of higher n modes, this process is observed for only $n \leq 25$, whereas the spectrum broadening is observed throughout the range of n. The effects of direct nonlinear couplings in the evolution of the $m = 1$ tearing modes are apparent in Fig. 18, which compares the quasilinear growth rates at $t = 600\,\tau_A$ of Fig. 17 with the instantaneous, nonlinear, magnetic energy growth rates at the same time. Figure 18 shows that the broadening of the $m = 1$ spectrum is mainly nonlinearly driven. To investigate this point further, a quasilinear calculation was carried out by including just 41 modes [Case 4, the $(0;0)$ average field together with $(m = 1; n = 1$–$40)]$. Case 4 was initialized identically to Case 1. The $m = 1$ magnetic energy spectrum is plotted in Fig. 19 for the nonlinear calculation Case 1 at $t = 650\,\tau_A$ and for the quasilinear calculation Case 4 at $t = 700\,\tau_A$. The lack of spectral spreading observed in the quasilinear calculation persists even at 2000 τ_A, which shows that this spreading is primarily a result of nonlinear couplings.

The modes which directly couple to the $m = 1$ perturbations are those having $m = 0$ and $m = 2$. In particular, the $(1; n)$ and $(1; n')$ are directly coupled by the $(2; n + n')$ and the $(0; |n - n'|)$, and adjacent modes ($n' = n + 1$) are thus coupled by the $(2; 2n + 1)$ and $(0; 1)$. In previous work,[5,6] the main effect of the $m = 2$ modes upon the $m = 1$ instabilities was shown to provide the energy sink necessary for a nonlinear saturation mechanism based on cascading to short wavelengths. This cascade is initiated by the generation of stable $m = 2$ current sheets. We seek to determine here whether the $m = 0$ or the $m = 2$ modes (or both) are principally responsible for broadening of the spectrum. Figure 7 shows that the magnetic energy stored in the $m = 0$ modes somewhat exceeds that contained in the $m = 2$ modes and that the difference increases slightly in time. Linear calculations of the $m = 0$ and $m = 2$ modes in the evolved average fields show that both types remain stable (and are hence driven) throughout the calculation. Comparing the radial structure of the $(0; 1)$ and $(2; 23)$ modes (Fig. 20) shows that the $(0; 1)$ has larger amplitude and more global extent than the $(2; 23)$. This follows from the fact that the $(0; 1)$ is directly coupled to, and hence **driven** by, every adjacent pair of unstable $(1; n)$ and $(1; n + 1)$, whereas the $(2; 2n + 1)$ is driven only by a single adjacent pair, $(1; n)$ and $(1; n + 1)$. For example, of all adjacent pairs of $m = 1$ modes, only the $(1; 11)$ and $(1; 12)$ drive the $(2; 23)$, but all adjacent unstable $(1; n)$ and $(1; n + 1)$ drive the $(0; 1)$. Although the $m = 1$ instabilities are not localized at their singular radii (Fig. 2), their amplitudes do peak in that vicinity (Fig. 11); direct coupling of adjacent unstable $m = 1$ modes should therefore provide the strongest drive for the $(0;1)$ and $(2;2n + 1)$.

To test the effect of the $m = 0$ modes and $m = 2$ modes on the broadening of the $m = 1$ spectrum, we carried out three calculations (see Table 1) similar to Case 1 except for mode selection. In the first calculation (Case 2), the $m = 0$, 1, and 2 modes are retained from Case 1, but $m \geq 3$ modes are eliminated. By comparison of this 136-mode calculation with Case 1, the effect of the high-m turbulent background and the previously predicted stabilizing cascade process to high-m modes are studied. The second calculation (Case 5) differs from Case 2 in the elimination of the $(m = 0; n \neq 0)$ modes; thus, only the $(0; 0)$ and $m = 1$ and $m = 2$ modes are retained, and a 121-mode calculation results. The deleted modes in the third calculation (Case 3) in relation to Case 2 are the $m = 2$ modes that which couple the adjacent $m = 1$ modes [$(2; n)$ with n odd], while the $m = 2$, even-n modes are retained. Case 3 results in a 96-mode calculation. Figure 21 shows the energy-weighted width in n, defined in Eqs. (15) and (16), of the $m = 1$ magnetic energy spectrum as a function of time for Case 2 and Case 5. For Case 2 this evolution is essentially identical to that for Case 1 (the 546-mode calculation). However, the broadening of the spectrum is delayed by more than $200\,\tau_A$ for Case 5. When the same quantities are compared for

Case 3, in which the $(m = 2; n$ odd) modes are deleted, the results agree identically with those of Case 2 through $t = 625\,\tau_A$, and even at $650\,\tau_A$ the difference is very slight. Hence, the rapid spreading of the spectrum to high n (and in r toward the field-reversal surface) is caused by the $(m = 0; n \neq 0)$ modes, which nonlinearly couple the $m = 1$ instabilities.

Let us now consider the nonlinear physics that is elucidated by these studies. The broadening of the $m = 1$ spectrum is a consequence of quasilinear "mode competition" and nonlinear interaction. However, comparison of quasilinear numerical calculations (Case 4), which retain $m = 1$ and $(m = 0; n = 0)$ evolution only, with corresponding full nonlinear calculations (Case 1) indicates that nonlinear coupling processes are dominant. Indeed, the $m = 1$ spectrum is strongly affected by nonlinear interaction with the $(0; 1)$ mode because neighboring $(1; n_0)$ and $(1; n_0 + 1)$ modes beat together to drive $(0; 1)$ and $(2; 2n_0 + 1)$ modes. The $(2; 2n_0 + 1)$ mode is a localized, stable, driven current sheet that transfers $m = 1$ energy to small-scale dissipation. In contrast, the driven $(0; 1)$ mode is global, with stability maintained by strong magnetic shear at the reversal surface. It back-reacts with the $(1; n_0 + 1)$ to drive the $(1; n_0 + 2)$. As a result, the $m = 1$ spectrum broadens. The radial spreading of the turbulent zone is, in turn, a consequence of the generation of $m = 1$ modes with progressively higher n and lower resonant $q(r_0)$ values and therefore larger singular radii. This process of nonlinear-mode competition can thus be represented as:

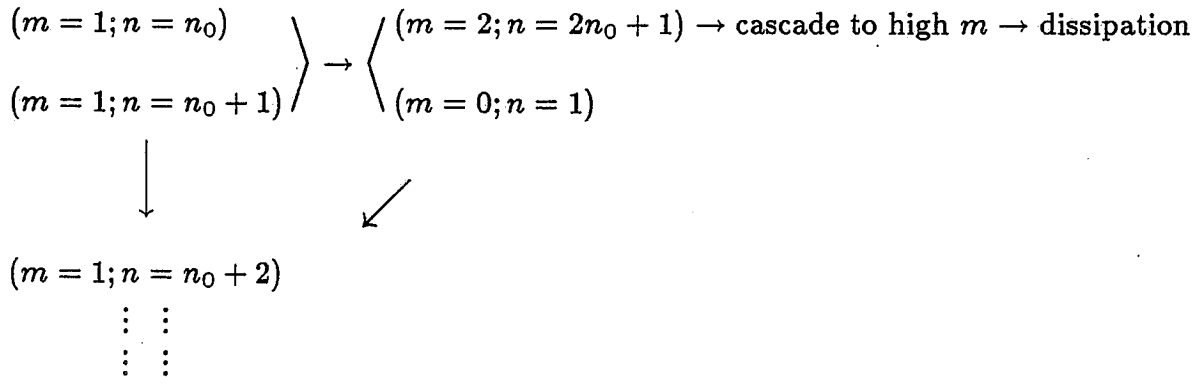

Note that the radially extended structure of the $m = 0$ mode is crucial to this mechanism since only such an extended mode can couple to $(m = 1; n = n_0, n_0 + 1,$ and $n_0 + 2)$.

Theoretical insight into the role of the $m = 0$ mode in $m = 1$ dynamics can be gained by using the energy spectrum equations from renormalized turbulence theory[5,8] for MHD turbulence in current-carrying plasma. Because the region of resonant tearing mode interaction is located well inside the field-reversal surface, where $\langle B_z \rangle > \langle B_\theta \rangle$, the reduced MHD equations for tokamaks[9] constitute an adequate plasma model. With standard methods[8] it follows that the equations for kinetic and magnetic energies, where $\mathrm{k} = (m; n)$,

are:

$$\frac{\partial}{\partial t}E_{\mathbf{k}}^{K} = i\int dx\,\widetilde{\Phi}_{-\mathbf{k}}k_{\|}\widetilde{J}_{\mathbf{k}} - \int dx\,\langle\widetilde{\Phi}\nabla_{\theta}\widetilde{\Psi}\rangle_{\mathbf{k}}\frac{d}{dx}\langle J\rangle + \int dx\sum_{\mathbf{k}'}\left(1-\frac{n'^{2}}{n''^{2}}\right)\Delta'_{\mathbf{k}''}\frac{\delta(x'')}{\Delta\omega_{\mathbf{k}''}}I(\mathbf{k}',\mathbf{k}) \tag{18}$$

and

$$\frac{\partial}{\partial t}E_{\mathbf{k}}^{B} = i\int dx\,\widetilde{J}_{-\mathbf{k}}k_{\|}\widetilde{\Phi}_{\mathbf{k}} - \frac{\eta}{S}\int dx\,\langle\widetilde{J}^{2}\rangle_{\mathbf{k}} + \int dx\left[\sum_{\mathbf{k}'}\frac{n^{2}}{n''^{2}}\Delta'_{\mathbf{k}''}\frac{\delta(x'')}{\Delta\omega_{\mathbf{k}''}}I(\mathbf{k},\mathbf{k}') - \frac{\Delta'_{\mathbf{k}}}{\Delta\omega_{\mathbf{k}}}\delta(x)\sum_{\mathbf{p}+\mathbf{q}=\mathbf{k}}I(\mathbf{p},\mathbf{q})\right], \tag{19}$$

where

$$I(\mathbf{r},\mathbf{s}) = \left[\left\langle\left(\nabla_{\theta}\widetilde{\Psi}\right)^{2}\right\rangle_{\mathbf{r}}\left\langle\left(\nabla_{x}\widetilde{\Phi}\right)^{2}\right\rangle_{\mathbf{s}} + \left\langle\left(\nabla_{\theta}\widetilde{\Phi}\right)^{2}\right\rangle_{\mathbf{r}}\left\langle\left(\nabla_{x}\widetilde{\Psi}\right)^{2}\right\rangle_{\mathbf{s}}\right]. \tag{20}$$

In Eqs. (18)–(20), $x = r - r_{\mathbf{k}}$, where r is the radial coordinate and $r_{\mathbf{k}}$ is the singular radius associated with the mode $\mathbf{k}$, the quantity $\mathbf{k}''$ is given by $\mathbf{k}'' = \mathbf{k} + \mathbf{k}'$ (thus, $n'' = n + n'$), and $\langle f\rangle_{\mathbf{k}}$ indicates the $\mathbf{k}$ component of the field f. The notations for the fields in Eqs. (18)–(20) are consistent with that in Eqs. (1)–(12) provided the limit $\langle B_z\rangle \gg \langle B_\theta\rangle$ is taken. In particular, J denotes the parallel current, which becomes J_z in the relevant limit. The quantities $\Delta'_{\mathbf{k}}$ denote the discontinuity of the radial derivative of $\widetilde{\Psi}_{\mathbf{k}}$ at the singular surface and are a straightforward generalization of the linear MHD stability parameters. The quantities $\Delta\omega_{\mathbf{k}}$ are the nonlinear decorrelation rates, which are amplitude dependent and (for $\Delta'_{\mathbf{k}''} < 0$) are given by

$$\Delta\omega_{\mathbf{k}} \approx \sum_{\mathbf{k}'}\frac{|\Delta'_{\mathbf{k}''}|\,\delta(x'')}{\Delta\omega_{\mathbf{k}''}}\left\langle\left(\nabla_{\perp}\widetilde{\Psi}\right)^{2}\right\rangle_{\mathbf{k}'}, \tag{21}$$

where $x'' = r - r_{k''}$. Let us now apply this model to the interpretation of the nonlinear process of the $m = 1$ spectral broadening. In particular, the $(0;1)$ mode is driven by coherent scattering from the $(1;n_0)$ off the $(1;n_0+1)$ mode. Similarly, the $(1;n_0+2)$ mode is driven by incoherent emission from the beating of the $(1;n_0+1)$ mode with the

(0; 1) mode. With the model of Eqs. (18)–(21), these two nonlinear interaction processes appear in the mode energy evolution equations as:

$$\frac{\partial}{\partial t} E_{1n_0} \cong \int dx\, \Delta'_{(0;1)} \frac{\delta(x'')}{\Delta\omega_{(0;1)}} I\left[(1;n_0),(1;n_0+1)\right] \tag{22}$$

and

$$\frac{\partial}{\partial t} E_{1n_0+2} \cong -\int dx \frac{\Delta'_{(1;n_0+2)}}{\Delta\omega_{(1;n_0+2)}}\, \delta(x)\, I\left[(1;n_0+1),(0;1)\right] \ , \tag{23}$$

respectively. It is important to note that $\Delta'_{(0;1)} < 0$, $\Delta'_{(2;n)} < 0$, and $\Delta'_{(1;n)} < 0$ for $n > 21$ (i.e., the $m = 1$ modes with higher n's are linearly stable but nonlinearly driven). As a consequence of the global character of the $m = 0$ mode, $m = 1$ interaction with $m = 0$ is stronger than with $m = 2$, as discussed previously. However, it is clear from Eqs. (22) and (23) that the nonlinear interaction terms are of opposite sign, and cancellation would thus result if an n summation were performed. This result, which follows from energy conservation, indicates that the principal role of interaction with the $(m = 0; n = 1)$ mode is to *redistribute* $m = 1$ mode energy among different n's.

Let us now consider the effect of the $m \geq 2$ perturbations. As shown in Fig. 20, these higher m modes are stable (hence driven), localized current sheets. In previous work,[5,6] it was proposed that these modes provide a nonlinear saturation mechanism by sinking energy from the $m = 1$ instabilities via a cascade of localized, driven current sheets of progressively finer scale. Indeed, it follows from Eqs. (18)–(20) that the effect of $m = 2$ interaction on $m = 1$ evolution is given by

$$\frac{\partial}{\partial t} E_{1n_0} = \int dx \sum_{\substack{m=1 \\ n=n'}} \Delta'_{(2;n_0+n')} \frac{\delta(x'')\, I\left[(1;n_0),(1;n_0+1)\right]}{\Delta\omega_{(2;n_0+n')}} \ , \tag{24}$$

where $\Delta'_{m=2} < 0$ indicates that $m = 2$ modes will draw energy **from** $m = 1$ modes. Furthermore, upon summation over n_0, it is apparent that interaction with $m = 2$ modes is a genuine $m = 1$ mode energy **sink** [i.e., $\partial/\partial t\,(E_{m=1}) < 0$]. However, the previous calculations,[6] with a full set of MHD equations, could include only a small number ($\lesssim$70) of modes. Here, this mechanism is reexamined numerically for cases with a large number of modes. The results are shown in Fig. 5, which plots the total magnetic fluctuation energy for several calculations, including Case 1 (546 modes), the reduction of Case 1 to Case 2 (136 modes) by deleting all $m \geq 3$ modes, the reduction of Case 2 to Case 3 (96 modes) by deleting all ($m = 2; n$ odd) modes, and finally the quasilinear run (Case 4) having the (0; 0) and $m = 1$ modes only.

Beginning with the quasilinear calculation (Case 4) there is a saturation of the total magnetic fluctuation energy, along with a slight spreading of the $m = 1$ spectrum with

little change after $t = 700\tau_A$ (the calculation was continued beyond $2000\tau_A$). Case 3 (96 modes) adds to the quasilinear calculation the $(m = 0; n \neq 0)$ modes, together with the $(m = 2, n$ even) harmonics of the $m = 1$ modes. This calculation incorporates the $m = 1$ spectrum broadening effects due to the $m = 1$ modes but not the direct coupling of adjacent $m = 1$ instabilities by $m = 2$ modes. The addition of these nonlinear coupling terms leads to a higher saturation energy as well as the spectrum broadening discussed above. Case 2 (136 modes) adds the $(m = 2; n$ odd) modes to the 96-mode calculation. Specifically, this amounts to the incorporation of the $m = 2$ perturbations that couple adjacent $m = 1$ modes. Compared with the 96-mode calculation, the total fluctuation energies are the same until after $t = 600\tau_A$, beyond which nonlinear effects lead to a lower saturation level for Case 2. This lowering of the magnetic energy saturation level, by nearly a factor of 2, is consistent with the discussion of the nonlinear saturation mechanism of the driven $m = 2$ current sheets presented in Refs. 5 and 6. Case 1 (546 modes), the calculation discussed in Sec. IV, is obtained from Case 2 (136 modes) by the addition of higher $m = 3$–5 perturbations. Again, the fluctuation energy closely follows that of Case 2 and Case 3 until $600\tau_A$. After this time, the nonlinear interactions involving the high-m modes become sufficiently strong that the total fluctuation energy saturates at a level below that of Case 2 and more than a factor of 2 below that of Case 3. This is again consistent with the model of Refs. 5 and 6, which depicts the higher m modes as localized, driven current sheets that draw energy from the $m = 1$ modes in a progressive cascade, resulting in lower saturation levels of the instability. This stabilization can be seen in the $m = 1$ spectra, compared for Case 2 (136 modes) and Case 1 (546 modes) at $t = 672\tau_A$ in Fig. 15. Except for fine detail, the high-n tails for the two cases are of the same level, and the most significant difference is a narrower and slightly lower peak for the dominant $n \approx 9$–13 modes in Case 1.

The $m = 1$ spectrum broadening discussed here also contributes to the cascade stabilization process. Because the $m = 1$ spectrum broadens, the $m = 2$ driven mode spectrum also broadens, and net $m = 1$ damping via nonlinear coupling to smaller scales is thus facilitated. Hence, the $(m = 0; n = 1)$ interaction also serves to accelerate the true nonlinear saturation mechanism. Indeed, the slow decay of the E_m^B spectrum [see Eq. (14) and Fig. 7] is consistent with the notion of cascade to small scales.

The $m = 1$ spectral-broadening process discussed here is important also to the mechanism of $\langle B_z(r)\rangle$ reversal and maintenance. In a previous investigation,[5] resistive kinks were shown to induce an electric field $\langle E_\theta(r)\rangle$ that acts to sustain the reversed $\langle B_z\rangle$ configuration. In particular, near the reversal surface, a quasilinear calculation of $\langle E_\theta(r)\rangle$

induced by stationary resistive kink turbulence predicts that

$$\langle E_\theta(r)\rangle = -\left\{\sum_n [1-nq(r)]\frac{|\,\widehat{\xi}_{(1;n)}(r)\,|^2}{r}\Delta\omega_{(1;n)}(r)\right\}\langle B_\theta(r)\rangle\ , \tag{25}$$

where $\widehat{\xi}$ is the radial component of the displacement vector. A crucial element in this expression is the nonlinear decorrelation rate (inverse lifetime) $\Delta\omega_{(1;n)}(r)$. In particular, $\Delta\omega_{(1;n)}(r)$ acts as a phase shift, which ensures that kink-induced reversal is "locked in" by nonlinear interaction and ultimately reconnection. The key question is: How is reversal driven by $m=1$ modes resonant in the core locked in at the reversal surface? The answer to this is revealed by examination of $\Delta\omega_{(1;n)}$:

$$\begin{aligned}\Delta\omega_{(1;n)}(r) = \sum_{n'}\Bigg\{&\frac{|\,\Delta'_{(0;1)}\,|}{\Delta\omega_{(0;1)}}\delta(r-r_{(0;1)})+\\ &\frac{|\,\Delta'_{(2;2n'+1)}\,|}{\Delta\omega_{(2;2n'+1)}}\delta(r-r_{(2;2n'+1)})\Bigg\}\times\langle(\nabla_\perp\psi)^2\rangle_{(1;n')}\ .\end{aligned} \tag{26}$$

Noting that the $(m=2;n=2n'+1)$ contribution is negligible at $r=r_{\rm rev}$ ($m=2$ modes are strongly localized), we see clearly that the required mechanism is reconnection due to the nonlinearly excited $(m=0;n=1)$ mode; i.e.,

$$\Delta\omega_{(1;n)} \cong \sum_{n'}\frac{|\,\Delta'_{(0;1)}\,|}{\Delta\omega_{(0;1)}}\langle(\nabla_\perp\psi)\rangle^2_{(1;n')}\,\delta(r-r_{(0;1)})\ . \tag{27}$$

Note that the radially extended structure of the $m=1$ and $m=0$ modes thus allows magnetic topology changes at $r=r_{\rm rev}$ because of excitations resonant in the core. Furthermore, since all parts of neighboring $(m=1;n=n_0)$ and $(m=1;n=n_0+1)$ modes drive the $(m=0;n=1)$, **all** $m=1$ modes contribute to the locking-in of reversal driven by resistive kinks. Thus the dynamo mechanism is a consequence of the nonlinear dynamics of the system and cannot be fully described in a quasilinear framework.

In summary, there are two major nonlinear couplings of $m=1$ instabilities which have significant effects on evolution in RFP plasmas. The coupling of $m=1$ instabilities by driven $m=0$ modes redistributes energy that leads to $m=1$ spectrum broadening in mode number and radius. The coupling by driven, localized $m=2$ current layers initiates a cascade to high-m modes, which constitutes a nonlinear saturation mechanism for the dominant instabilities. Physical consequences of these processes include the locking in of the reversed magnetic field by reconnection associated with the $(0;1)$ mode and a broad turbulent zone that should have a negative effect on confinement.

VI. CONCLUSIONS

The nonlinear dynamics of tearing modes was studied numerically for a reversed field pinch configuration with an emphasis on understanding the mechanisms for the development of the broad, turbulent spectrum and the saturation of the perturbations in a turbulent quasi-steady state. These two nonlinear physical processes were shown to be the result of the two interaction mechanisms of the $m = 1$ instabilities, with coupling to driven $m = 0$ modes leading to $m = 1$ energy redistribution and coupling to driven $m = 2$ localized current sheets leading to saturation. With a reduced system of resistive MHD equations, which behaves much as a full compressible system of equations for force-free equilibria, the effects of the driven $m = 0$ and $m \geq 2$ modes upon the $m = 1$ instabilities were studied. These effects were isolated in controlled numerical experiments by comparing the results of calculations retaining different sets of modes. The results show that the $(m = 0; n \neq 0)$ perturbations are primarily responsible for the broadening of the perturbation spectrum to high n and hence from the plasma core radially outward toward the field-reversal surface and that the $m \geq 2$ modes provide a nonlinear saturation mechanism for the $m = 1$ instabilities. The spectral broadening is facilitated by the radially extended structure and large amplitude of the $m = 0$ modes [the $(0; 1)$ is driven by all adjacent pairs of unstable $m = 1$ modes], which redistribute the $m = 1$ energy to higher n, as shown by energy conservation arguments. As the $m = 1$ spectrum broadens, so does the spectrum of the $m = 2$ modes, which are localized current sheets driven by the adjacent $m = 1$ modes. The effect of these and higher m modes is a nonlinear saturation mechanism that involves the dissipation of the energy of the original $m = 1$ instabilities through a driven cascade to small-scale perturbations. The effect of changing the initial conditions in the calculation was to alter the dynamical evolution; however, for two very different choices of initial conditions, similar quasi-steady, turbulent states were eventually obtained. The physical consequences of these nonlinear processes include the locking in of the $\langle B_z(r) \rangle$ field reversal by reconnection associated with the $m = 0$ modes and the development of a broad turbulent region of enhanced transport processes.

FIGURE CAPTIONS

FIG. 1. Linear growth rates of the resistive $(m = 1; n)$ eigenfunctions plotted versus n for the equilibrium studied in this paper. These results were obtained using $S = 10^4$ and $\varepsilon_L = 0.2$.

FIG. 2. B_θ and v_z components of the $(m = 1; n = 11)$ eigenfunctions plotted as functions of radius for the same cases considered in Fig. 1.

FIG. 3. Magnetic island widths plotted as functions of time for a 1/10 single helicity calculation for the equilibrium considered in this paper, with $S = 10^4$ and $\varepsilon_L = 0.2$.

FIG. 4. Safety factor and toroidal (J_ζ) and poloidal (J_θ) current density profiles for the low-Θ equilibrium used in these calculations. This equilibrium has inverse aspect ratio $\varepsilon_L = 0.2$.

FIG. 5. Total magnetic fluctuation energies versus time for Cases 1–4 of Table I. These cases have identical initialization and differ in mode selection only.

FIG. 6. Magnetic energy E^B_{mn} versus n for $m = 1$ in Case 1 at three different times.

FIG. 7. Magnetic energy E^B_m in the m components versus m for Case 1 at the three times shown in Fig. 6.

FIG. 8. Magnetic field line (Poincaré) plots at six times for Case 1. The cross sections correspond to lengthwise slices through the cylinder in the $\theta = 0°$–$180°$ plane.

FIG. 9. Magnetic energy distribution widths versus time for poloidal mode numbers $m = 0$, 1, and 2 in Case 1. These widths are defined as the energy-weighted (E^B_{mn}) root mean squares of $n - \overline{n}$ and are plotted centered about $\overline{n}$, where $\overline{n}$ is the energy-weighted mean of n for each m.

FIG. 10. Magnetic energy E^B_{mn} versus n for $m = 5$ in Case 1 at two different times.

FIG. 11. B_θ components of the $(m = 1; n)$ modes for $n = 19$, 21, 25, and 29 at $t = 600\,\tau_A$ in Case 1.

FIG. 12. Radial distribution of magnetic energy in $m = 1$ components at two different times in Case 1.

FIG. 13. Parallel current density profile $J_\parallel/|\mathbf{B}|$ at $t = 680\,\tau_A$ in Case 1 compared with the equilibrium profile.

FIG. 14. Magnetic energy E^B_{mn} spectrum evolution for $m = 1$ versus n and t for Case 1.

FIG. 15. Magnetic energy E^B_{mn} versus n for $m = 1$ in Cases 1 and 2 at $t = 672\,\tau_A$.

FIG. 16. Magnetic energy E^B_{mn} versus n for $m = 1$ in Cases 2 and 6 at total energy saturation.

FIG. 17. Comparison of linear growth rates of the $(1; n)$ modes for the evolved average fields in Case 1 at $t = 600\,\tau_A$ and for the initial equilibrium.

FIG. 18. Comparison of the instantaneous linear and nonlinear growth rates of the $(1; n)$ modes in Case 1 at $t = 600\,\tau_A$.

FIG. 19. Comparison of the $m = 1$ magnetic energies E^B_{1n} for Case 1 at $t = 650\,\tau_A$ and Case 4 at $t = 700\,\tau_A$.

FIG. 20. B_z and B_θ components of the $(1; 0)$ and $(2; 23)$ modes, respectively, versus r for Case 1 at $t = 600\,\tau_A$.

FIG. 21: Magnetic energy distribution widths versus time for $m = 1$ modes in Case 2 (full nonlinear calculation) and Case 5 [$(m = 0; n \neq 0)$ modes absent].

TABLE 1. Mode selection for nonlinear calculations.

Case	$m = 0$	$m = 1$	$m = 2$	$m \geq 3$	Total Number of Modes	Comment
1	0–15	1–40	1–80	410 modes $m = 3, 4, 5$	546	Mode selection in text
2	0–15	1–40	1–80		136	
3	0–15	1–40	1–80 even		96	
4	0	1–40			41	
5	0	1–40	1–80		121	
6	0–15	1–40	1–80		136	Different initialization

REFERENCES

[1] R. G. Watt and R. A. Nebel, Phys. Fluids **26**, 1168 (1983).

[2] I. H. Hutchinson, M. Malacarne, P. Noonan, and D. Brotherton-Ratcliffe, Nuclear Fusion **24**, 59 (1984).

[3] E. J. Caramana, R. A. Nebel, and D. D. Schnack, Phys. Fluids **26**, 1305 (1983).

[4] H. R. Strauss, Phys. Fluids **27**, 2580 (1984).

[5] Z. G. An, P. H. Diamond, R. D. Hazeltine, J. N. Leboeuf, M. N. Rosenbluth, R. D. Sydora, T. Tajima, B. A. Carreras, L. Garcia, T. C. Hender, H. R. Hicks, J. A. Holmes, V. E. Lynch, and H. R. Strauss, in *Plasma Physics and Controlled Nuclear Fusion Research 1984*, IAEA-CN-44/E-III-10, (IAEA, Vienna, 1985) Vol. 2, p. 231.

[6] J. A. Holmes, B. A. Carreras, T. C. Hender, H. R. Hicks, V. E. Lynch, Z. G. An, and P. H. Diamond, Phys. Fluids **28**, 261 (1985).

[7] B. A. Carreras, M. N. Rosenbluth, and H. R. Hicks, Phys. Rev. Lett. **46**, 1131 (1981).

[8] P. H. Diamond, R. D. Hazeltine, Z. G. An, B. A. Carreras, and H. R. Hicks, Phys. Fluids **27**, 1449 (1984).

[9] H. R. Strauss, Phys. Fluids **19**, 134 (1976).

[10] J. A. Holmes, B. A. Carreras, T. C. Hender, H. R. Hicks, V. E. Lynch, and B. F. Masden, Phys. Fluids **26**, 2569 (1983).

[11] H. R. Hicks, B. A. Carreras, J. A. Holmes, D. K. Lee, and B. V. Waddell, J. Comput. Phys. **44**, 46 (1981).

[12] V. E. Lynch, B. A. Carreras, H. R. Hicks, J. A. Holmes, and L. Garcia, Computer Physics Communications **24**, 465 (1981).

[13] J. B. Taylor, Phys. Rev. Lett. **33**, 1139 (1974).

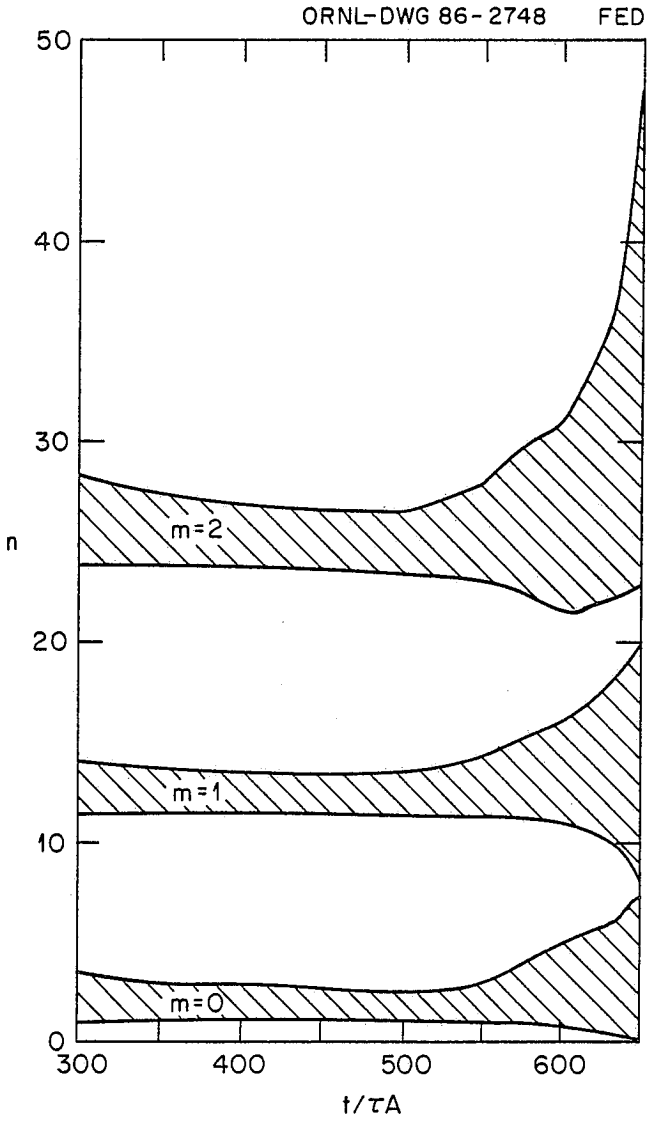
ORNL-DWG 86-2748 FED
50
40
30
20
10
0
n
m=2
m=1
m=0
300
400
500
600
t/τA

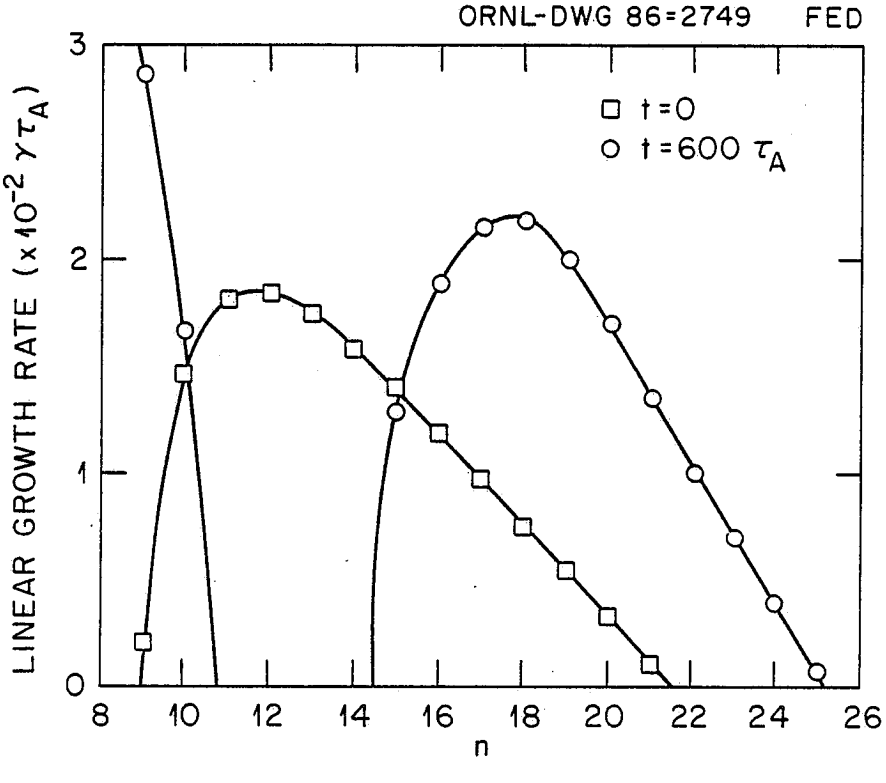
ORNL-DWG 86-2749 FED
□ t=0
○ t=600 τ_A
LINEAR GROWTH RATE ($\times 10^{-2}\ \gamma\tau_A$)
n
0
1
2
3
8
10
12
14
16
18
20
22
24
26

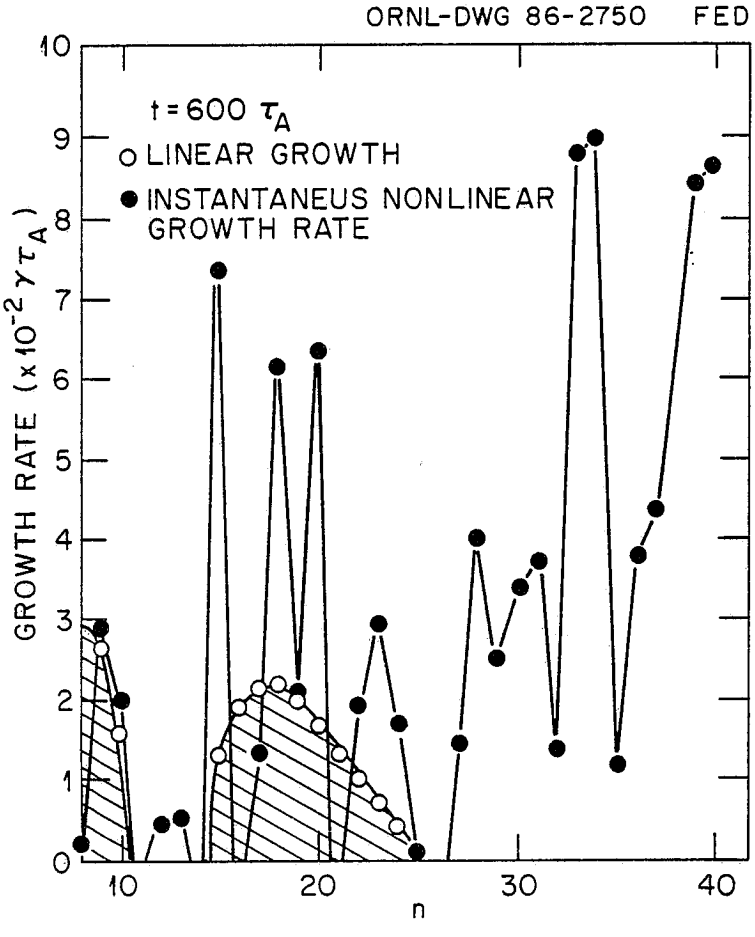
ORNL-DWG 86-2750 FED
t = 600 τ_A
o LINEAR GROWTH
● INSTANTANEUS NONLINEAR GROWTH RATE
GROWTH RATE ($\times 10^{-2} \gamma \tau_A$)
n
0
1
2
3
4
5
6
7
8
9
10
10
20
30
40

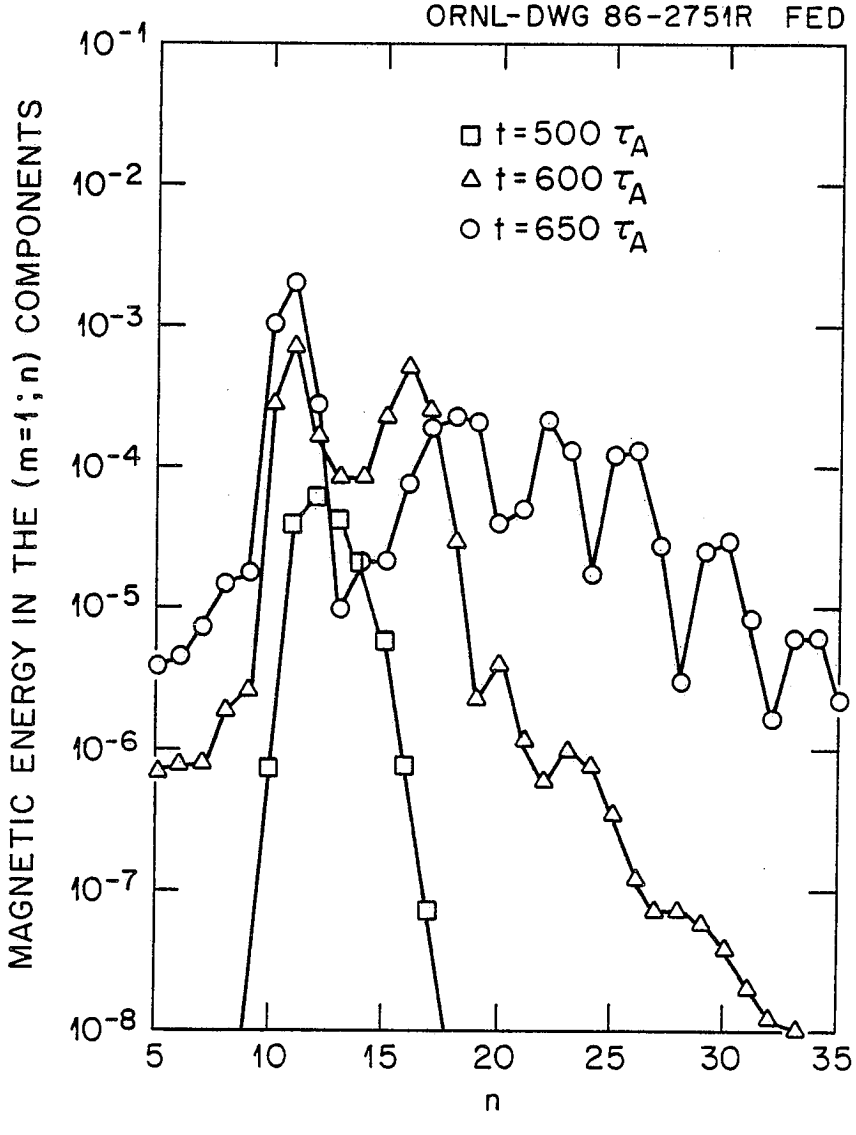
ORNL-DWG 86-2751R FED
MAGNETIC ENERGY IN THE (m=1; n) COMPONENTS
□ t=500 τ_A
△ t=600 τ_A
○ t=650 τ_A
10^{-1}
10^{-2}
10^{-3}
10^{-4}
10^{-5}
10^{-6}
10^{-7}
10^{-8}
5
10
15
20
25
30
35
n

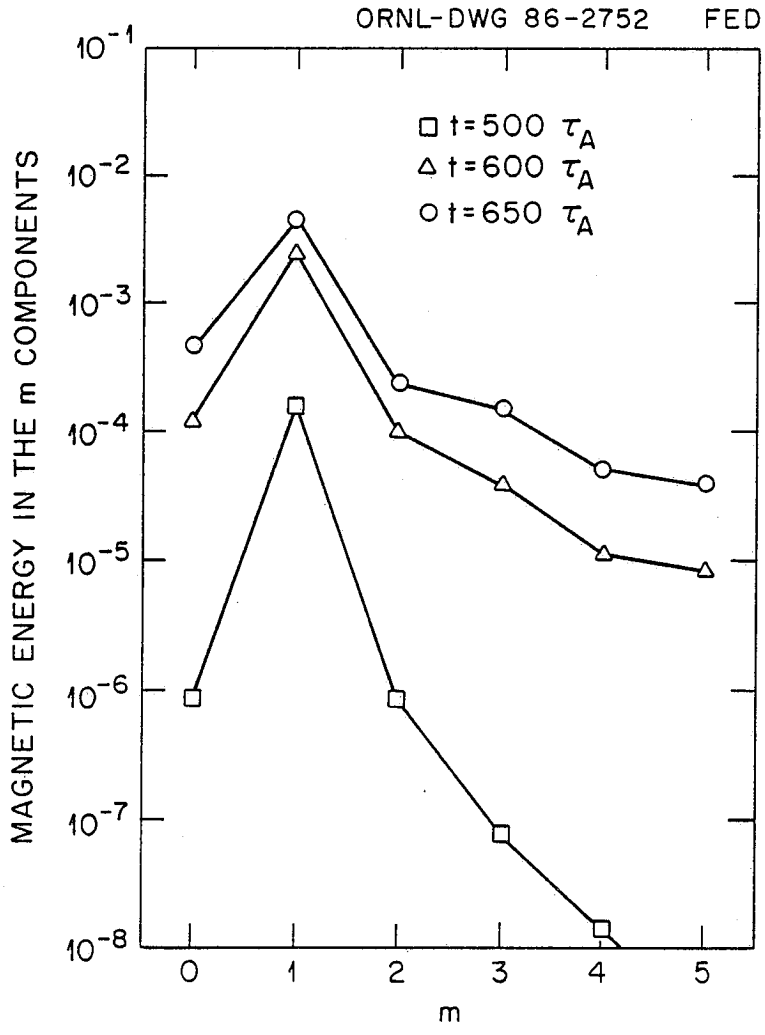
ORNL-DWG 86-2752 FED
MAGNETIC ENERGY IN THE m COMPONENTS
10^{-1}
10^{-2}
10^{-3}
10^{-4}
10^{-5}
10^{-6}
10^{-7}
10^{-8}
□ t=500 τ_A
△ t=600 τ_A
○ t=650 τ_A
0
1
2
3
4
5
m

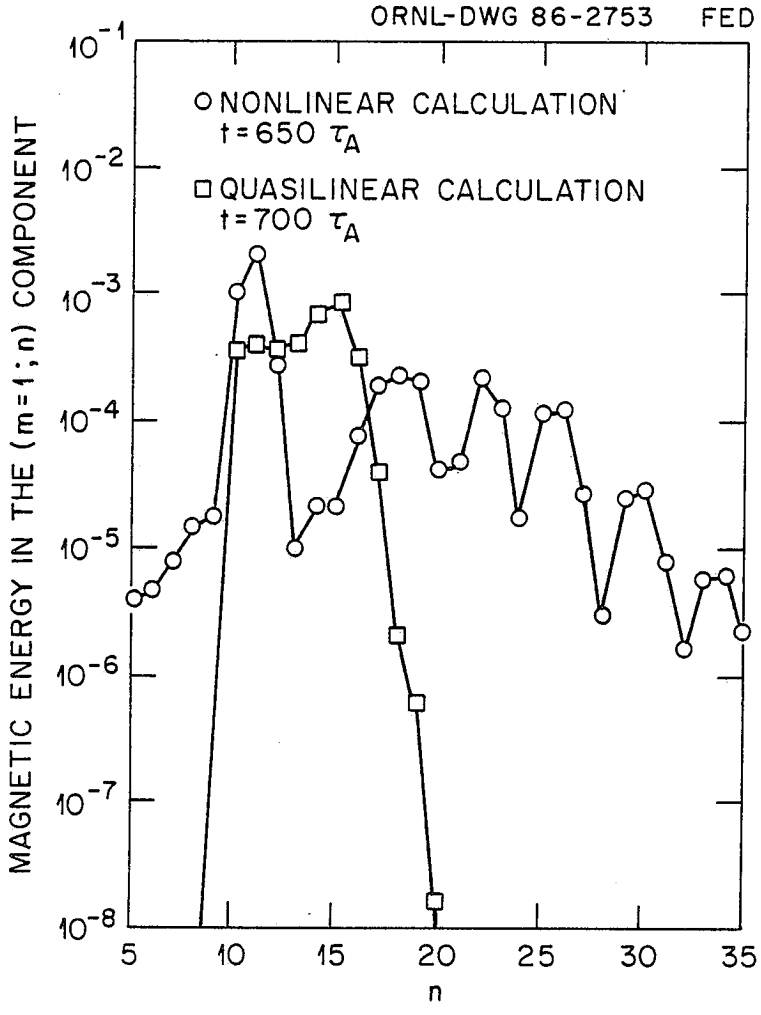
ORNL-DWG 86-2753 FED
NONLINEAR CALCULATION
t = 650 τA
QUASILINEAR CALCULATION
t = 700 τA
MAGNETIC ENERGY IN THE (m=1; n) COMPONENT
10^-1
10^-2
10^-3
10^-4
10^-5
10^-6
10^-7
10^-8
5
10
15
20
25
30
35
n

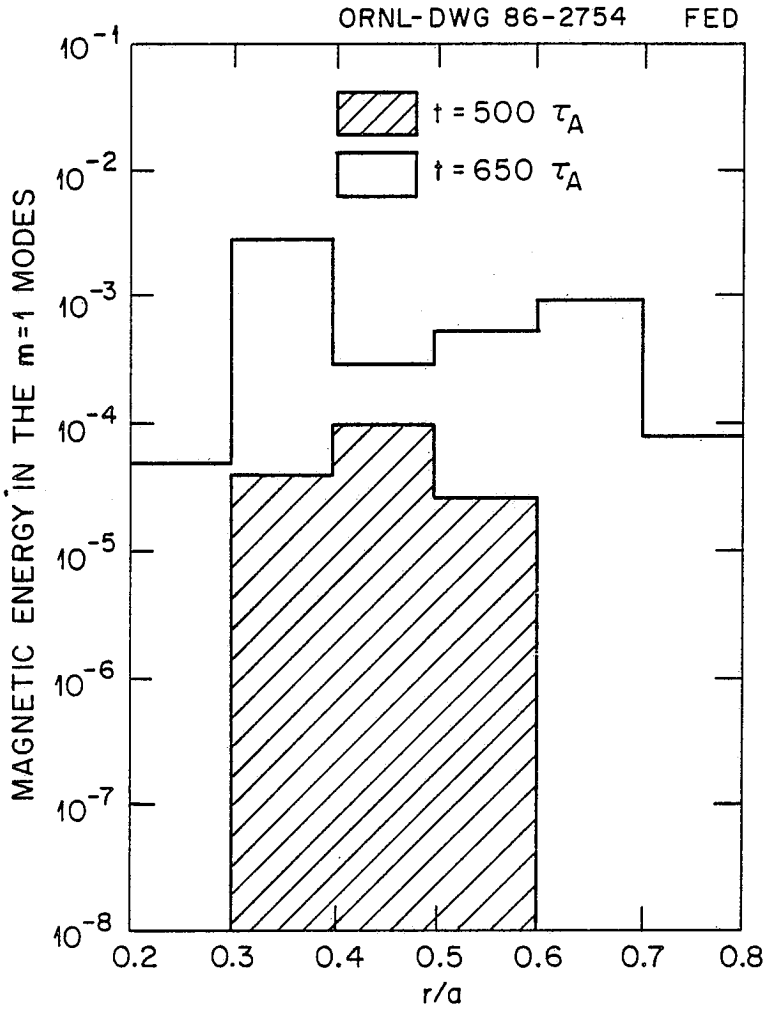
ORNL-DWG 86-2754 FED
t = 500 τ_A
t = 650 τ_A
MAGNETIC ENERGY IN THE m=1 MODES
10^{-1}
10^{-2}
10^{-3}
10^{-4}
10^{-5}
10^{-6}
10^{-7}
10^{-8}
0.2
0.3
0.4
0.5
0.6
0.7
0.8
r/a

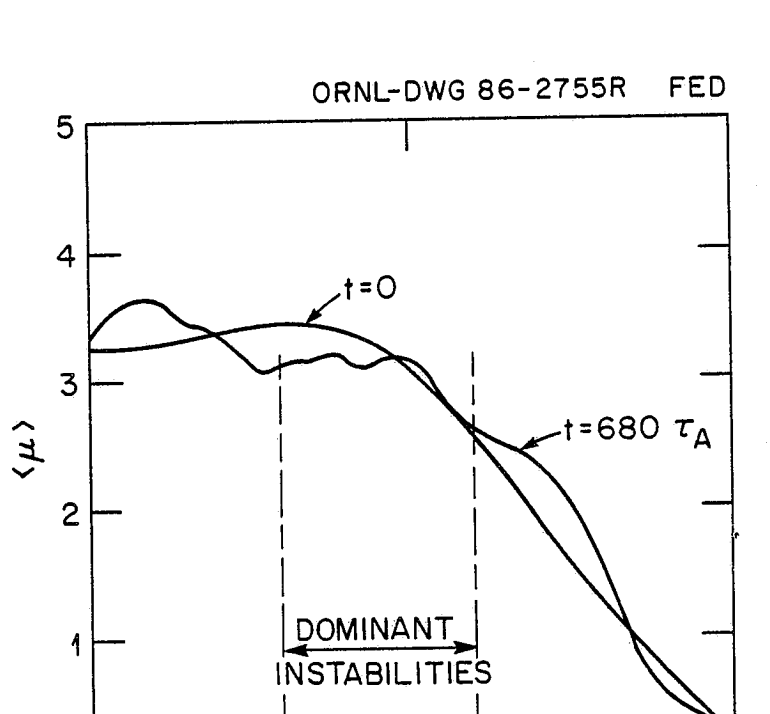
ORNL-DWG 86-2755R FED
5
4
3
2
1
0
0
0.5
1.0
r/a
⟨μ⟩
t=0
t=680 τA
DOMINANT
INSTABILITIES

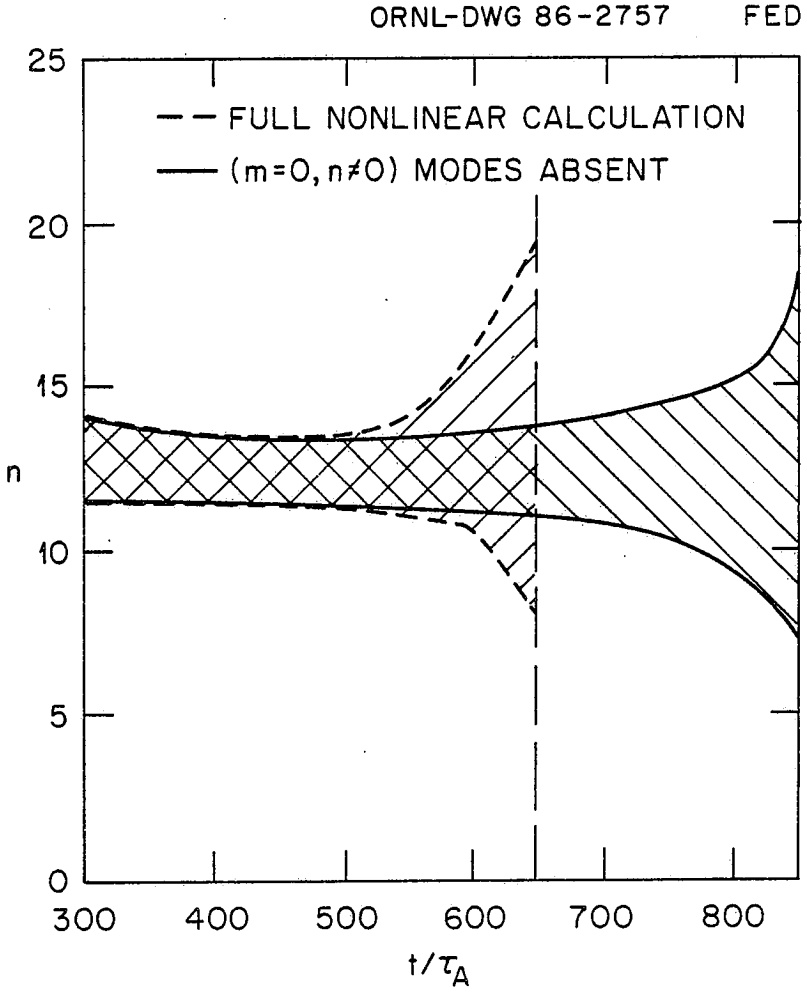
ORNL-DWG 86-2757 FED
FULL NONLINEAR CALCULATION
(m=0, n≠0) MODES ABSENT
25
20
15
10
5
0
n
300
400
500
600
700
800
t/τA

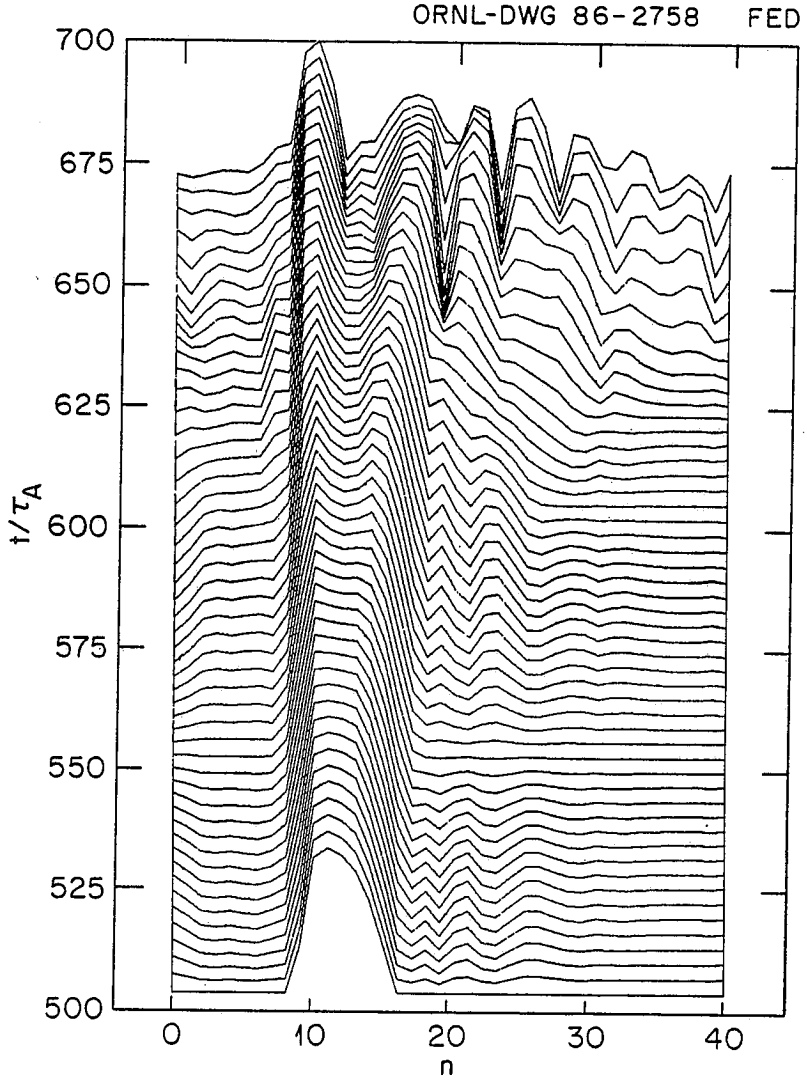
ORNL-DWG 86-2758 FED
700
675
650
625
600
575
550
525
500
t/τ_A
0
10
20
30
40
n

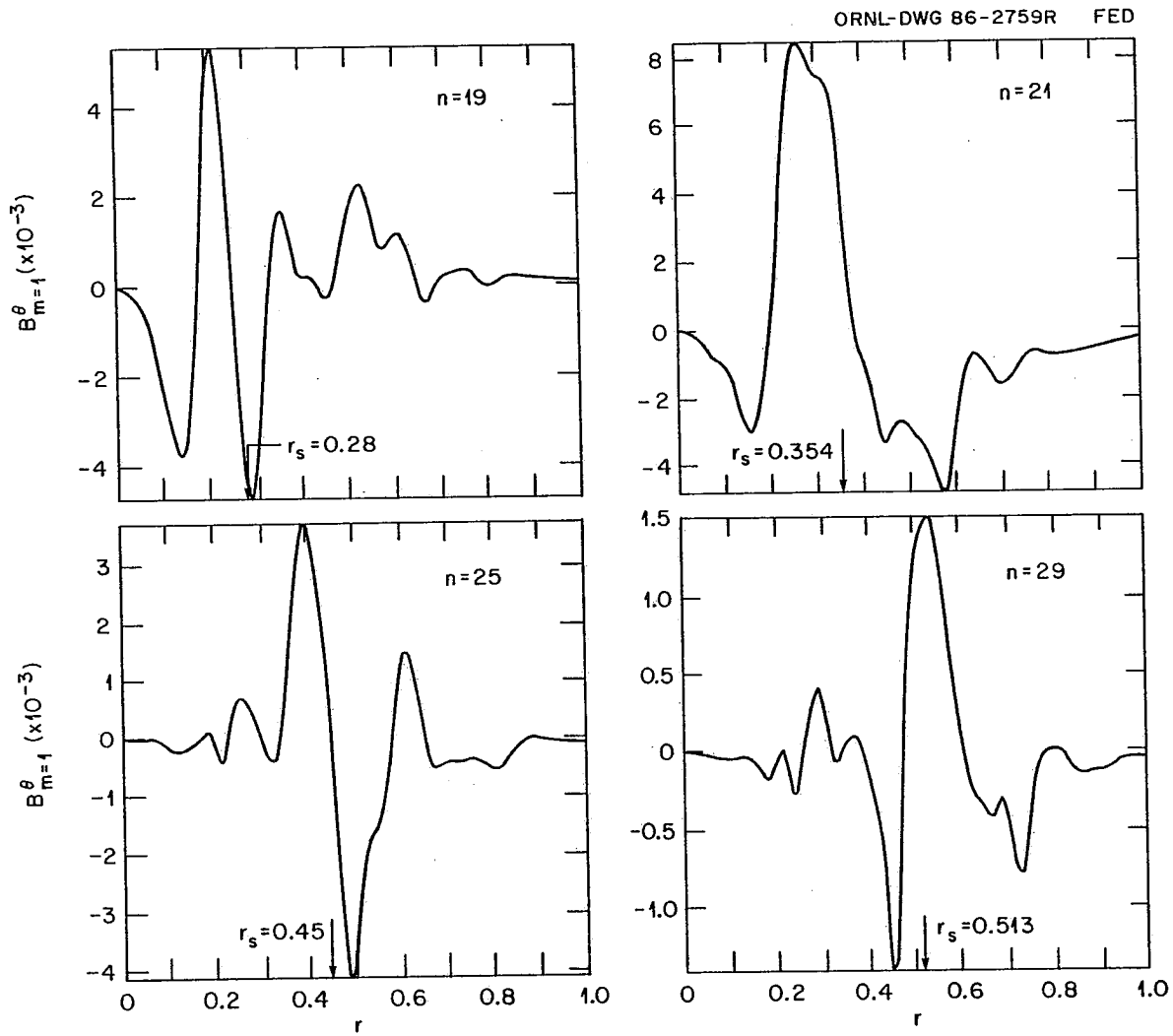
ORNL-DWG 86-2759R FED
n=19
r_s=0.28
n=21
r_s=0.354
n=25
r_s=0.45
n=29
r_s=0.513
$B^{\theta}_{m=1}$ (x10^{-3})
r

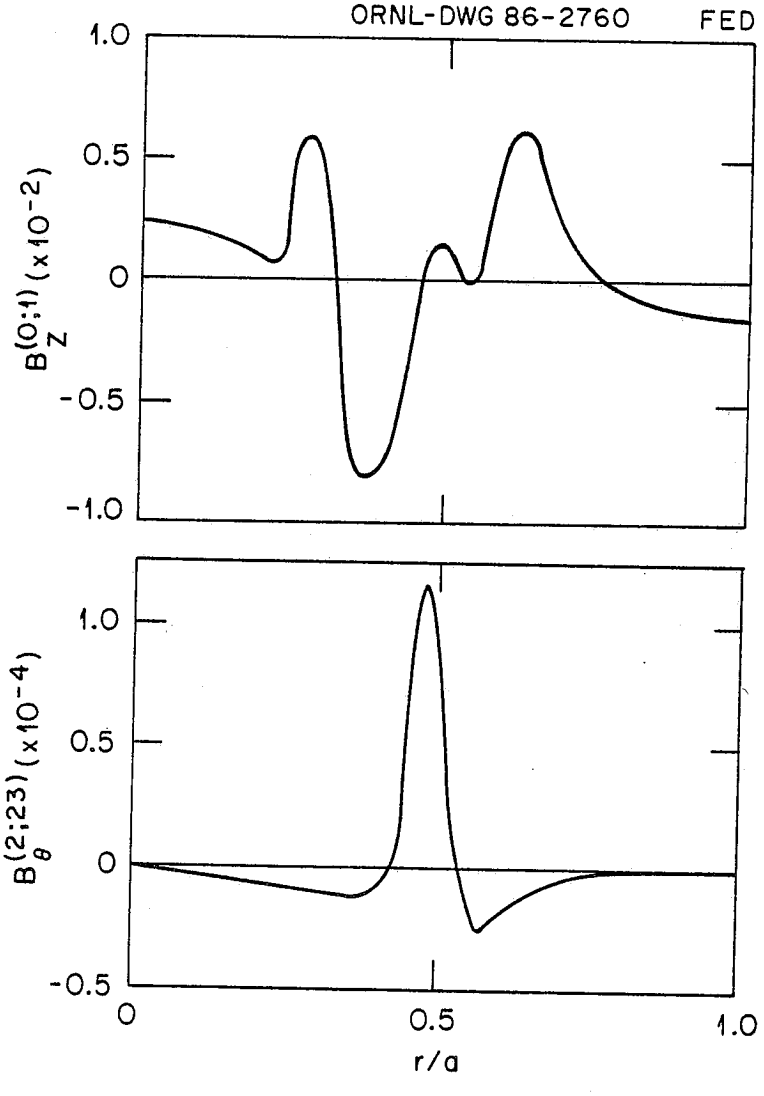
ORNL-DWG 86-2760
FED
1.0
0.5
0
-0.5
-1.0
$B_Z^{(0;1)}$ (x 10^{-2})
1.0
0.5
0
-0.5
$B_\theta^{(2;23)}$ (x 10^{-4})
0
0.5
1.0
r/a

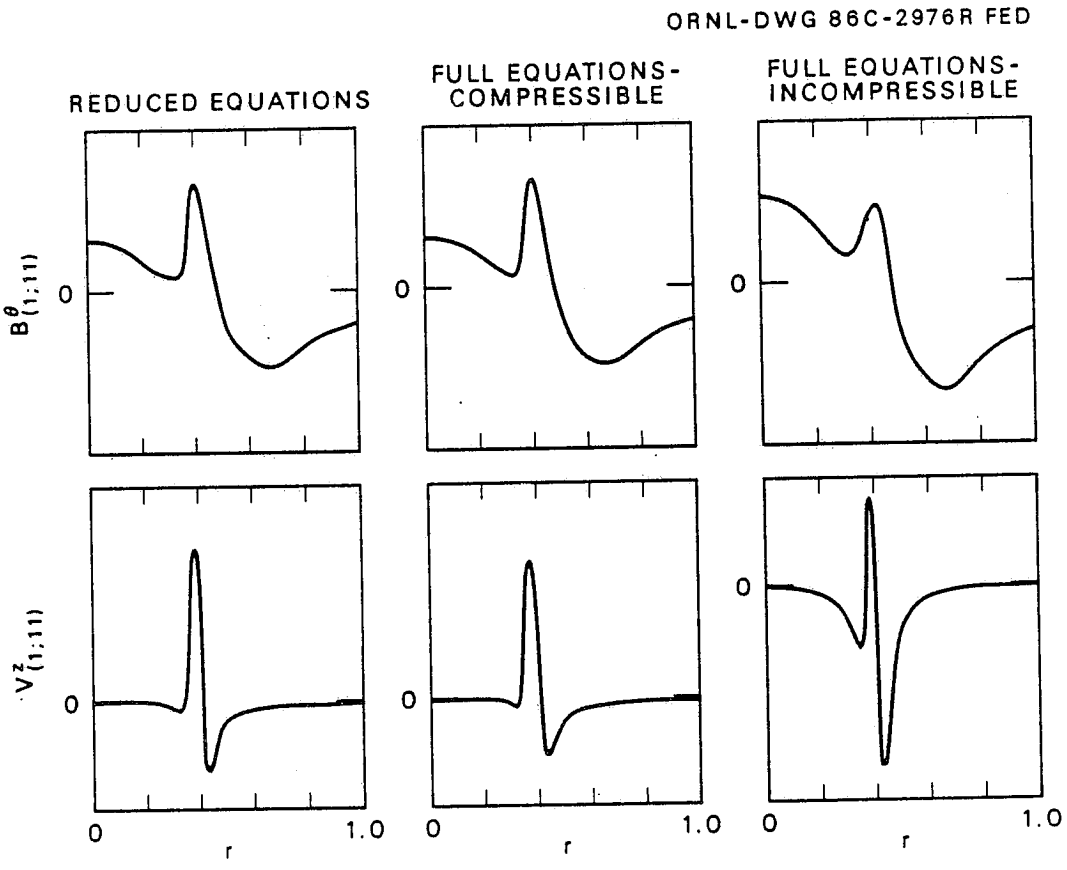
ORNL-DWG 86C-2976R FED
REDUCED EQUATIONS
FULL EQUATIONS-
COMPRESSIBLE
FULL EQUATIONS-
INCOMPRESSIBLE
$B^{\theta}_{(1;11)}$
$V^{z}_{(1;11)}$
0
0
0
0
0
0
0
1.0
0
1.0
0
1.0
r
r
r

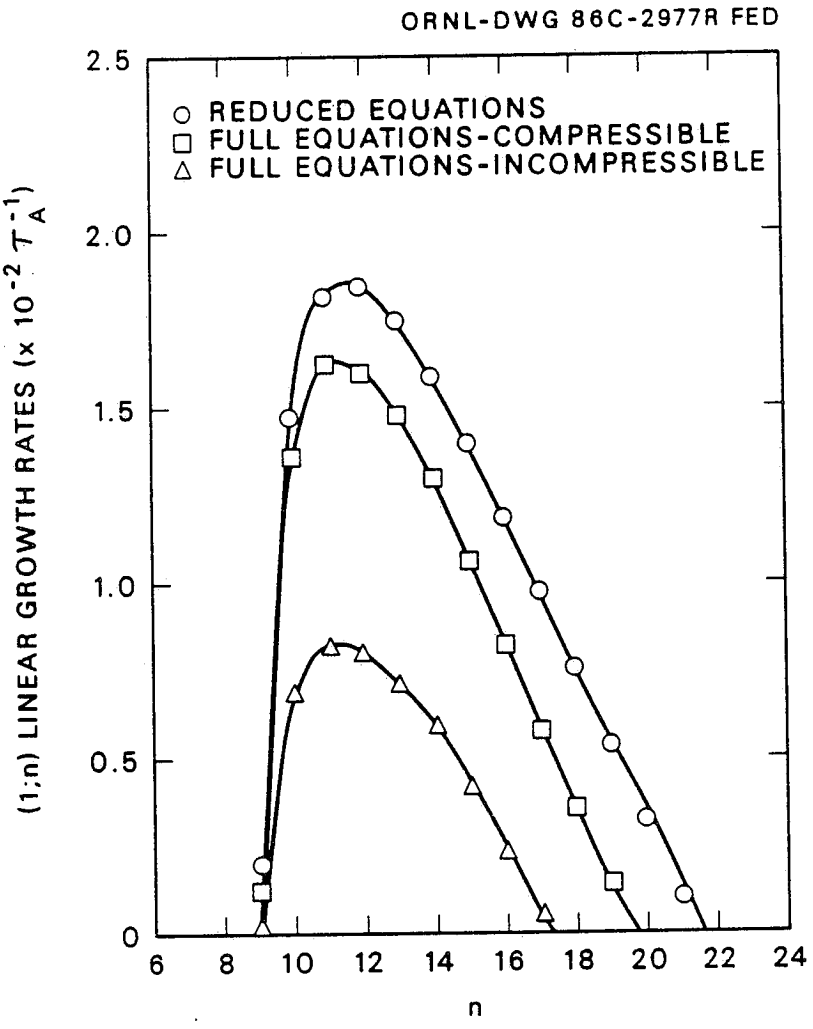
ORNL-DWG 86C-2977R FED
REDUCED EQUATIONS
FULL EQUATIONS-COMPRESSIBLE
FULL EQUATIONS-INCOMPRESSIBLE
(1;n) LINEAR GROWTH RATES (x 10^-2 τ_A^-1)
2.5
2.0
1.5
1.0
0.5
0
6
8
10
12
14
16
18
20
22
24
n

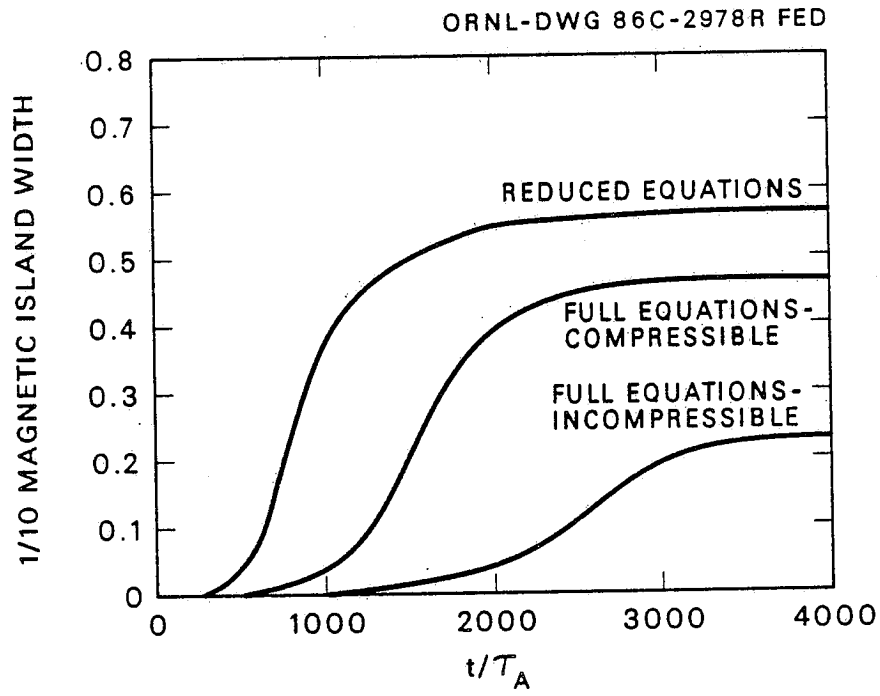
ORNL-DWG 86C-2978R FED
1/10 MAGNETIC ISLAND WIDTH
0.8
0.7
0.6
0.5
0.4
0.3
0.2
0.1
0
REDUCED EQUATIONS
FULL EQUATIONS-
COMPRESSIBLE
FULL EQUATIONS-
INCOMPRESSIBLE
0
1000
2000
3000
4000
t/τ_A

ORNL-DWG 86-2979 FED

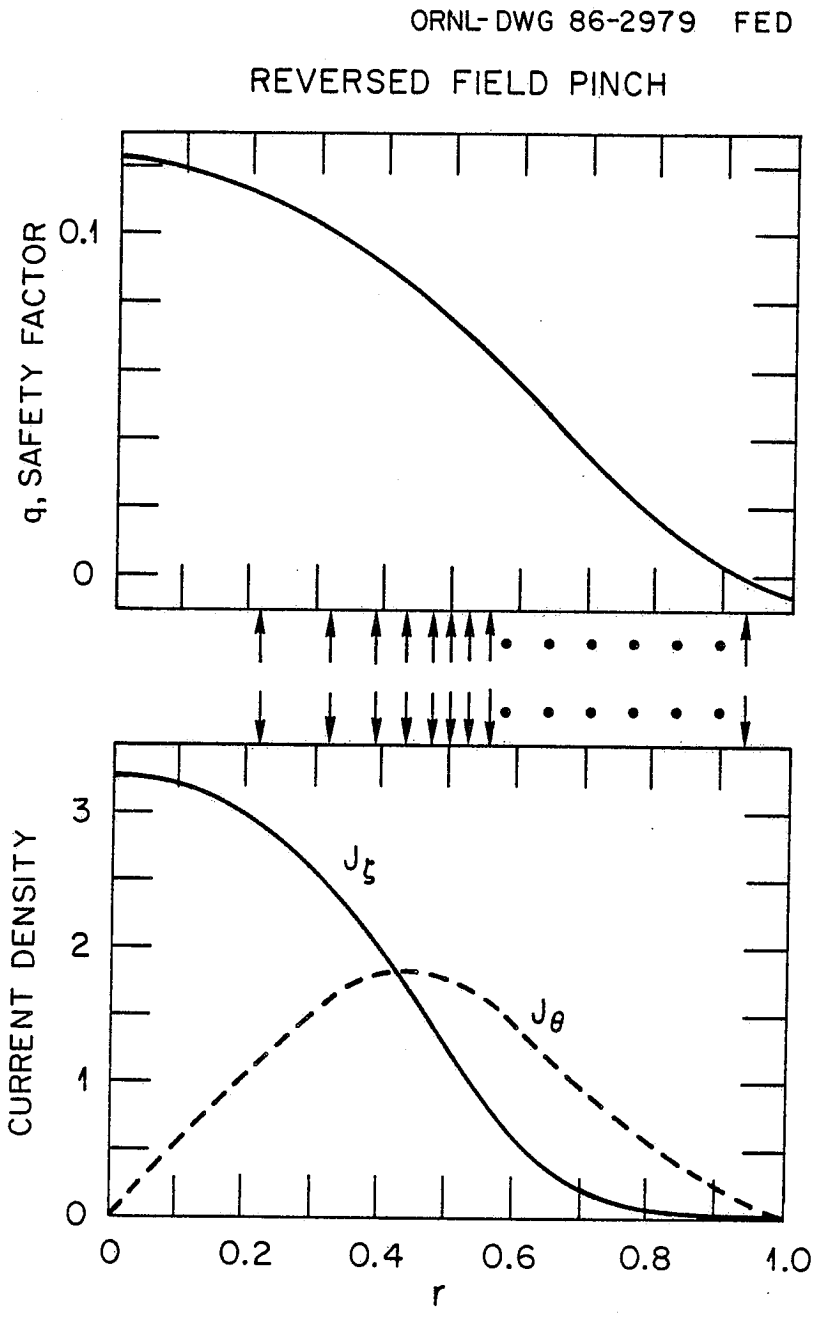

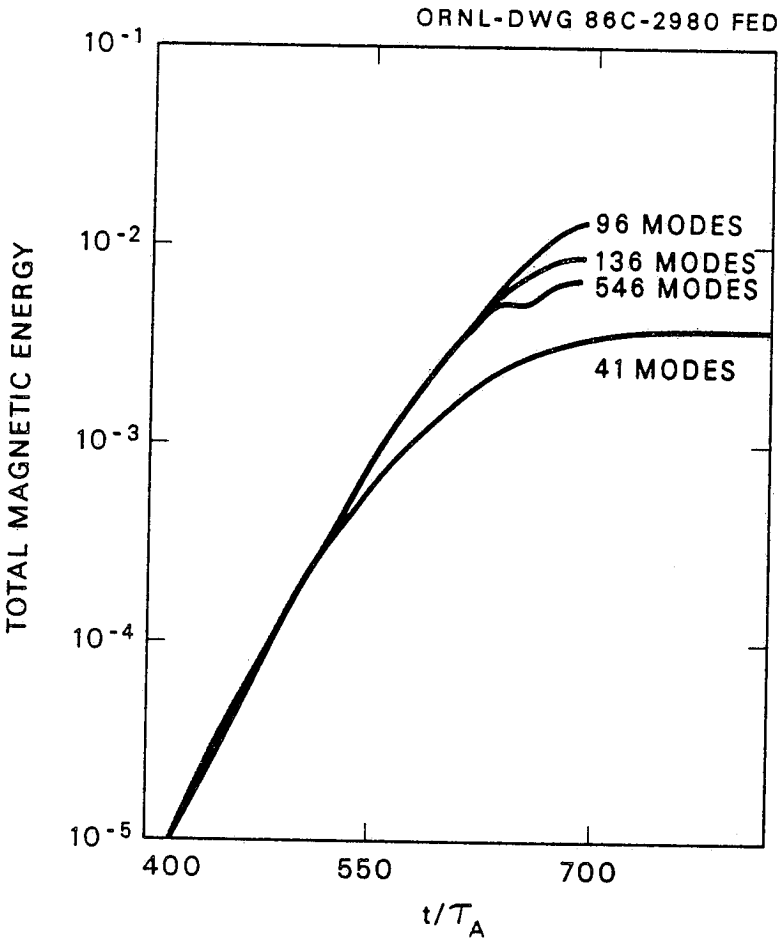
ORNL-DWG 86C-2980 FED
TOTAL MAGNETIC ENERGY
10^{-1}
10^{-2}
10^{-3}
10^{-4}
10^{-5}
96 MODES
136 MODES
546 MODES
41 MODES
400
550
700
t/τ_A

ORNL-DWG 86-2990R FED

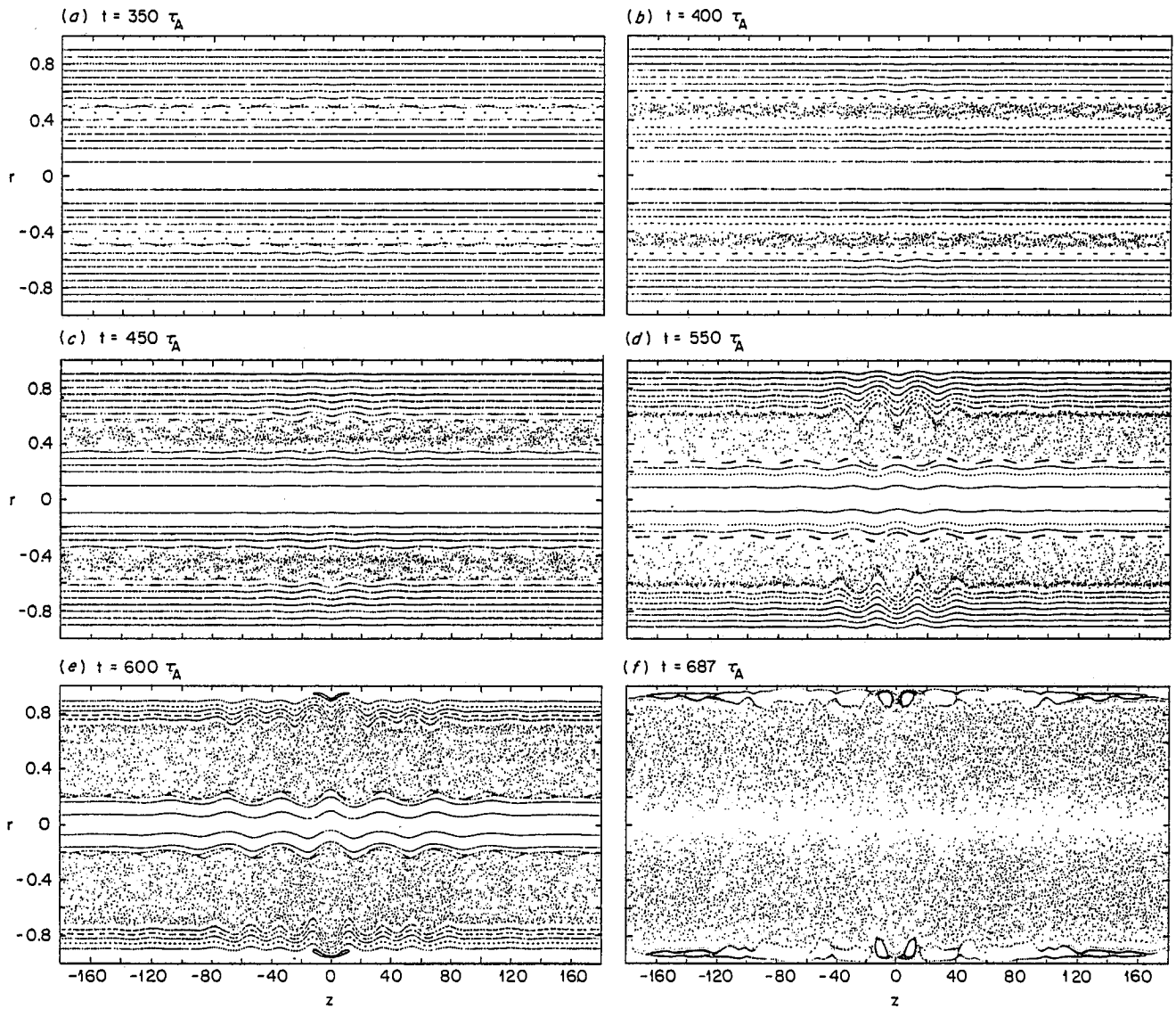

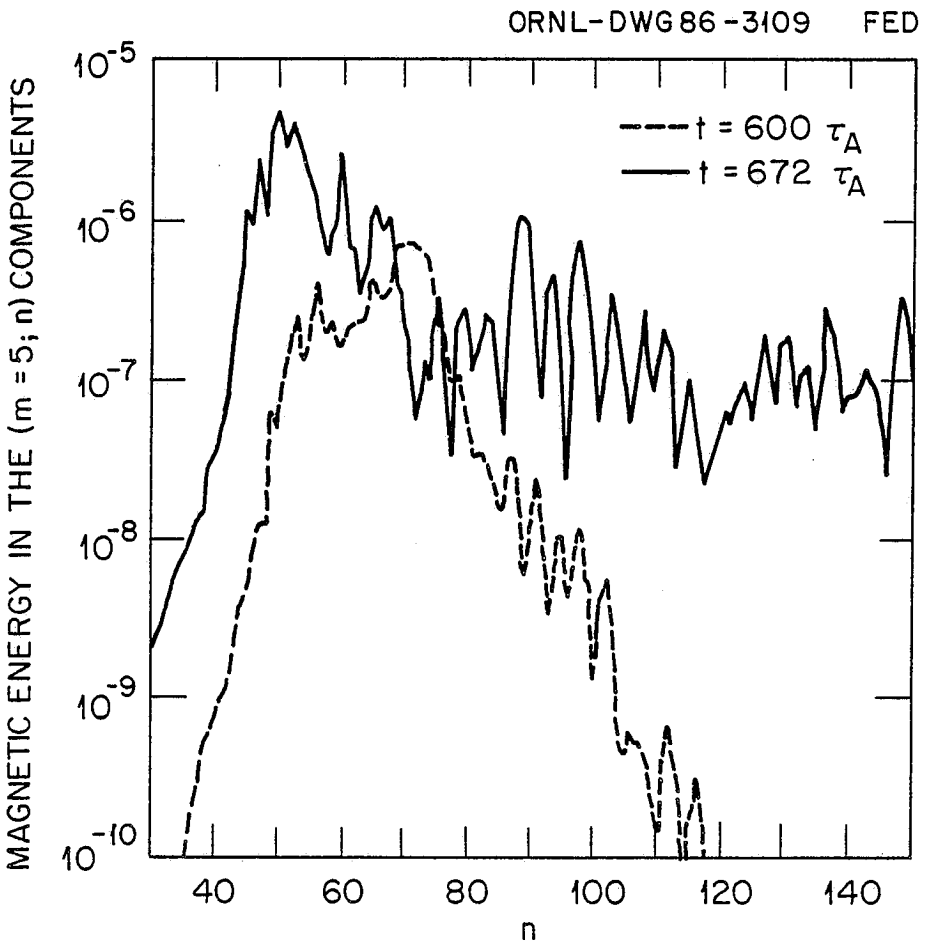
ORNL-DWG 86-3109 FED
MAGNETIC ENERGY IN THE (m = 5; n) COMPONENTS
10^{-5}
10^{-6}
10^{-7}
10^{-8}
10^{-9}
10^{-10}
t = 600 τ_A
t = 672 τ_A
40
60
80
100
120
140
n

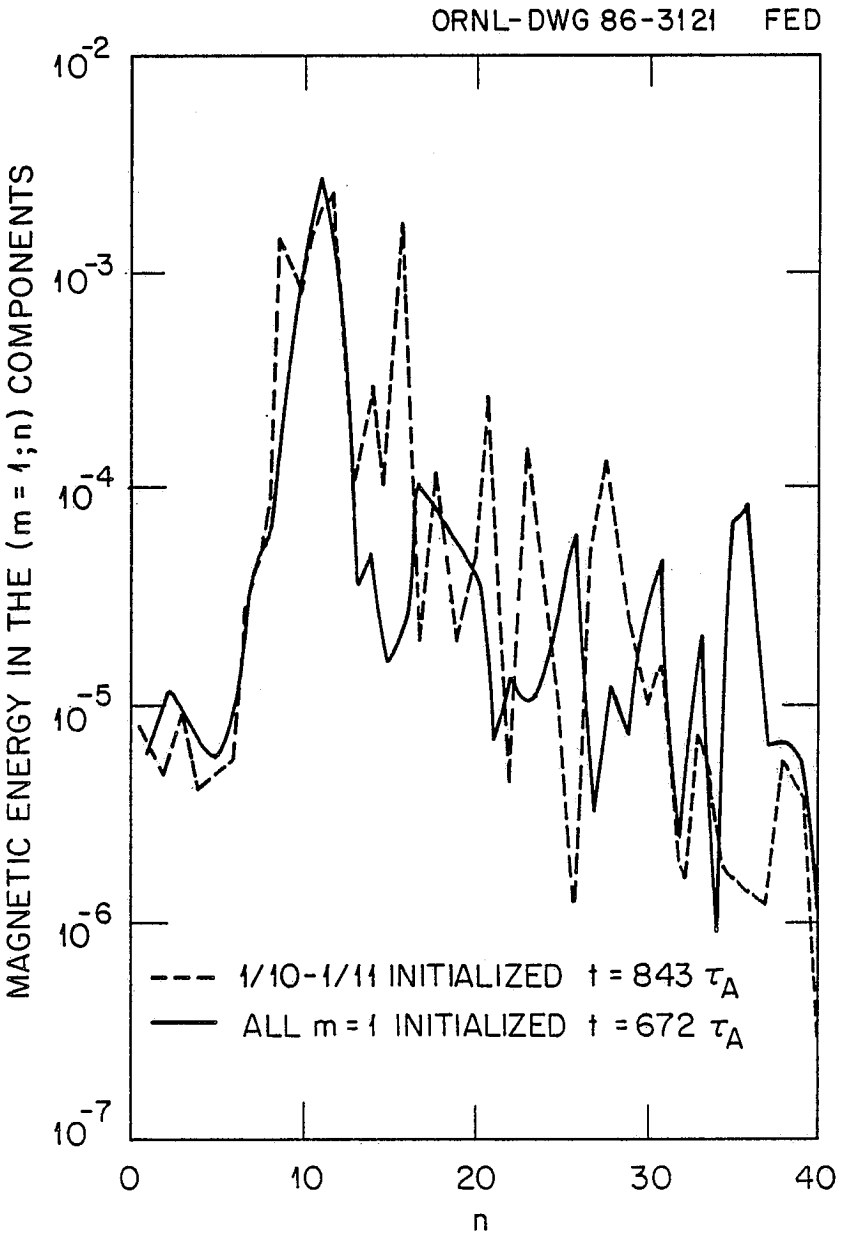
ORNL-DWG 86-3121 FED
MAGNETIC ENERGY IN THE (m = 1; n) COMPONENTS
10^{-2}
10^{-3}
10^{-4}
10^{-5}
10^{-6}
10^{-7}
0
10
20
30
40
n
1/10-1/11 INITIALIZED t = 843 τ_A
ALL m = 1 INITIALIZED t = 672 τ_A

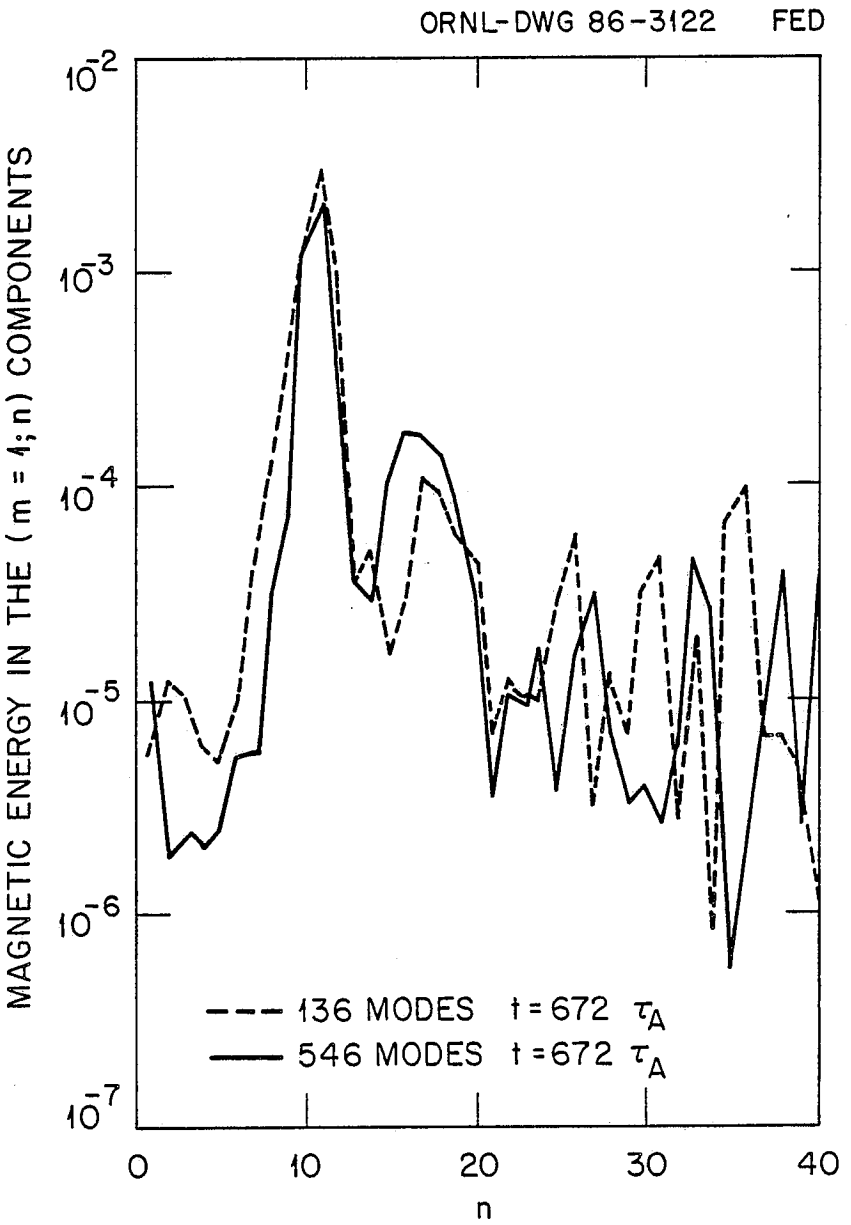
ORNL-DWG 86-3122 FED
MAGNETIC ENERGY IN THE (m = 4; n) COMPONENTS
10^{-2}
10^{-3}
10^{-4}
10^{-5}
10^{-6}
10^{-7}
0
10
20
30
40
n
136 MODES t = 672 τ_A
546 MODES t = 672 τ_A